CrossMark

REVIEW

Two-Dimensional Transition Metal Oxide and Chalcogenide-Based Photocatalysts
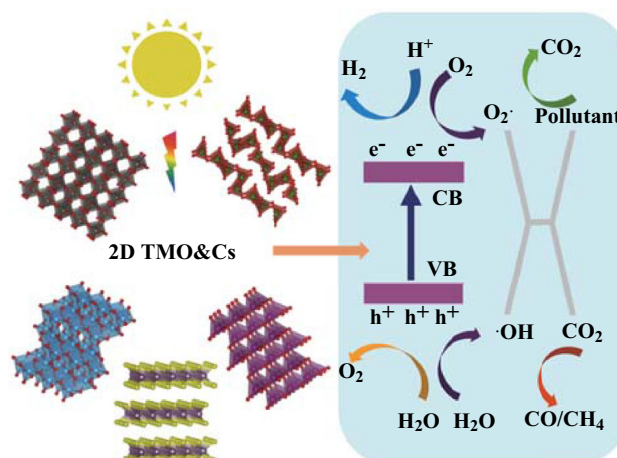
Farjana Haque[1] · Torben Daeneke[1] · Kourosh Kalantar-zadeh[1] · Jian Zhen Ou[1]

Highlights

- This review summarizes current two-dimensional (2D) transition metal oxide and chalcogenide (TMO&C)-based photocatalytic systems for hydrogen evolution reactions, organic pollutant degradation, carbon reduction and microbial disinfectants.
- The influences of unique features of 2D TMO&C in terms of crystal and electronic band structures are reviewed regarding their photocatalytic performances.
- The improvement strategies of 2D TMO&C photocatalysts including elemental doping, surface functionalization and heterojunction formation are critically discussed.

Abstract Two-dimensional (2D) transition metal oxide and chalcogenide (TMO&C)-based photocatalysts have recently attracted significant attention for addressing the current worldwide challenges of energy shortage and environmental pollution. The ultrahigh surface area and unconventional physiochemical, electronic and optical properties of 2D TMO&Cs have been demonstrated to facilitate photocatalytic applications. This review provides a concise overview of properties, synthesis methods and applications of 2D TMO&C-based photocatalysts. Particular attention is paid on the emerging strategies to improve the abilities of light harvesting and photoinduced charge separation for enhancing photocatalytic performances, which include elemental doping, surface functionalization as well as heterojunctions with semiconducting and conductive materials. The future opportunities regarding the research pathways of 2D TMO&C-based photocatalysts are also presented.

✉ Kourosh Kalantar-zadeh
  kourosh.kalantar@rmit.edu.au

✉ Jian Zhen Ou
  jianzhen.ou@rmit.edu.au

[1] School of Engineering, RMIT University, Melbourne, Australia

1 Introduction

Energy shortage and the environmental contamination are the current two of the most common challenges globally, which are mainly attributed to the rapid industrial development and population growth [1]. Therefore, the development of high efficiency, green energy and sustainable technologies for clean energy production and environmental remediation becomes an imperative task [1]. Sunlight is an abundant and easily available natural energy resource, which possesses great potential in driving environment-friendly photochemical reactions. The conversion of solar energy to chemical energy or solar fuels has been considered as one of the most prospective long-term solutions to solve global energy and environmental issues [1, 2]. Photocatalyst is the key to realize such a conversion [3, 4]. Common photocatalytic materials include metal-free organic compounds [5] and semiconductors [6–8], in which most of the interest has been focused on the semiconductor system. In such a system, upon the illumination of an appropriate light source with its energy equal or greater than the bandgap energy of the semiconductor, electrons are excited from the valence band (VB) to the conduction band (CB), inducing the formation of holes in the VB. Then, a fraction of photogenerated electrons and holes migrate to the surface of the semiconductor, while the rest recombine together, releasing the energy in the form of heat or photons [6]. Depending on the chemical potentials of the photoexcitons, various redox reactions can be occurred with absorbed species on the semiconductor surface. For instance, electrons with the potential above that of H_2/H_2O can produce H_2 gas by reacting with the water molecules in the surface of the semiconductor, while holes contribute to the O_2 production if their potential is below that of O_2/H_2O [3]. In the presence of CO_2 gas together with H_2O, the photogenerated electrons may participate in reducing CO_2 to CO, CH_4 or other forms of carbohydrates, competing with the H_2 production process due to the fact that the redox potentials for CO_2 reduction are close to that of H_2/H_2O [9]. On the other hand, the holes generated in the VB with the potential below that of OH^-/H_2O may react with surface-bound H_2O or OH^- to produce hydroxyl radicals, while the electrons in the CB are picked up by electron accepting species to generate radical anions [10]. The hydroxyl radicals and radical anions are the primary oxidizing species in the photocatalytic oxidation processes, which result in the removal of organic compounds (e.g., dyes, pesticides, phenols and other organic pollutants) and induce oxidative stress to the cell membrane of microbial organism [11–13].

Over the past few decades, a large amount of effort has been devoted to many semiconductors as possible candidates, in which most of them are in the forms of thin film, nanoparticle and one-dimensional (1D) nanostructures [14–16]. Single transition metal oxide (TMO) is the most popular category of photocatalytic semiconductors due to their low cost and excellent chemical stability. The representative candidates are TiO_2 and ZnO [8, 17–19]. According to Fig. 1, both chemical potentials of the CB and VB of these materials are thermodynamically favorable for many types for photocatalytic applications such as water splitting, pollutant degradation and microbial disinfection. However, their wide optical bandgaps (3.2–3.4 eV) restrict the light absorption only in the ultraviolet region (only 4% of solar spectrum). In addition, they are with low charge carrier mobility and high electron–hole pair recombination rates, which hinder their photocatalytic performances. Therefore, visible light-driven TMOs with relatively narrower bandgap energies are highly desired. For instance, WO_3, MoO_3 and V_2O_5 have the bandgap energies in the range between 2.6 and 3.0 eV, which lie in the visible light region and hence promote stronger absorption of photons. In addition, they have good electron transport properties that alleviate the characteristic of fast charge recombination which is commonly existed in TMOs [20–22]. But from band structure positions (Fig. 1), those may not be efficient photocatalysts because of their relatively low CB positions, resulting in ineffective consumption of photoinduced electrons during oxygen reduction reactions, and subsequently hinders oxidative degradation of pollutants by holes. Similar challenges are faced by other low bandgap TMOs such as CuO and Fe_2O_3 [6, 23–25].

Transition metal chalcogenides (TMCs) are also studied due to their earth abundance. CdS and ZnS are the two most studied materials [26–30]. CdS has a bandgap of 2.4 eV which potentially results in better visible light harvesting compared to many popular TMO-based photocatalysts (Fig. 1). In addition, its CB and VB positions are thermodynamically favorable for many photocatalytic applications. Unfortunately, the separation and transfer of photogenerated electron–hole pairs within the material are inefficient and it suffers from strong photocorrosion effect. In comparison, ZnS is mostly inert in corrosive environment and has the optimum band structures as well. However, its wide bandgap energy ($\sim$ 3.6 eV) results in poor visible light absorbability.

In addition to single transition metal oxides and chalcogenides (TMO&Cs), the photocatalytic properties of complex metal oxides and chalcogenides (e.g., binary and ternary metal compounds), nitrides, carbides and phosphides have also been widely studied. However, in this paper, we will not review this category of photocatalytic materials. For more details, readers can refer to some recently published works [31–34].
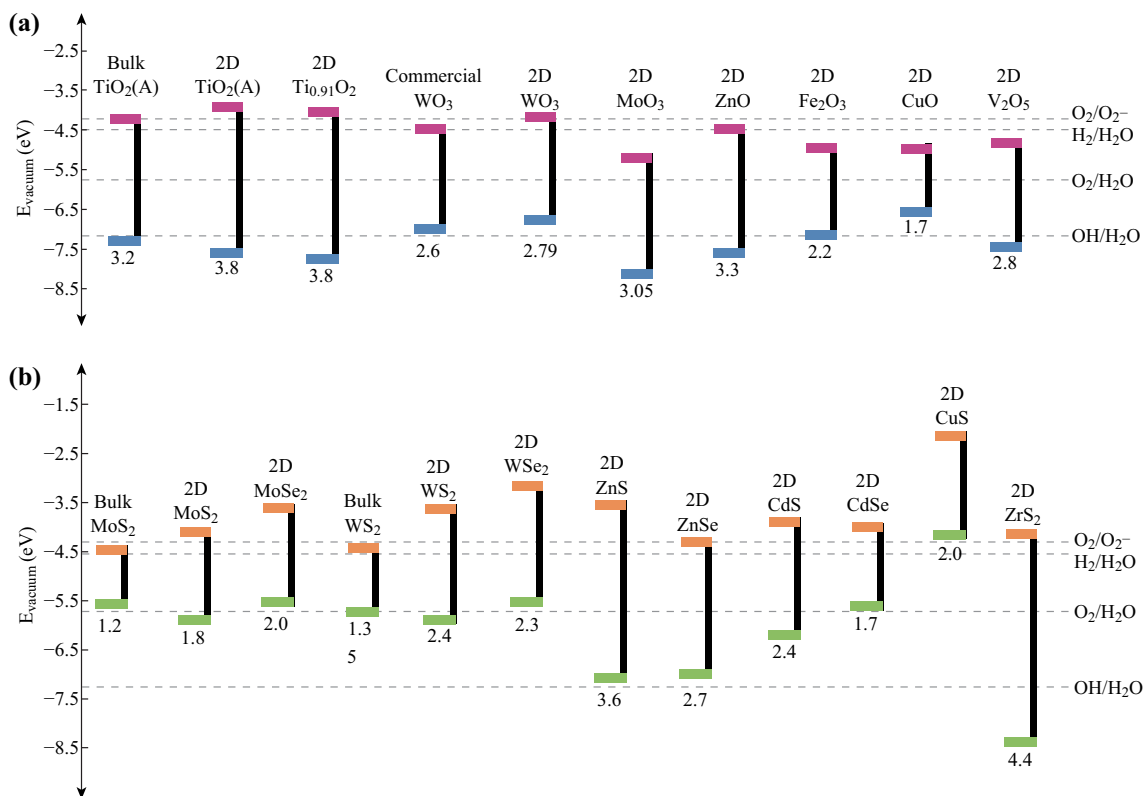
Fig. 1 Band structure of currently popular **a** transition metal oxides and **b** transition metal chalcogenides for photocatalytic applications [35, 103, 104, 202–210]

TMO&Cs in the form of two-dimensional (2D) planar structures are proven to be promising for photocatalytic applications. The larger surface area of 2D planar nanostructures can obviously provide more available active sites for catalytic redox reactions with surface absorbed species [35–37]. In addition, charge migration across both interfaces, i.e., catalyst–electrolyte and catalyst–charge collector, is also promoted, leading to the reduction in interfacial charge transfer resistance and improvement of photocatalytic reaction kinetics [38]. Furthermore, compared to the bulk counterpart, the atomic arrangements at the surface of 2D nanostructures are usually different, possibly due to the surface atomic elongation and structural disordering, which may affect the physical processes of charge transfer at the interface and the defect density [39, 40]. Therefore, the adsorbability of reactant ions or molecular species and the photocorrosion behavior will be significantly altered [39]. More importantly, the 2D planar configuration allows the dominant exposure of one particular facet with distinct atomic arrangement [40, 41], which is more suitable for the separation of photogenerated charge pairs and the utilization of photons. This is due to the fact that the flat band potential and the degree of band bending may be changed at the catalyst–electrolyte interface in the presence of Fermi-level pinning effect [41–43]. It is also well known

that the bandgap energies and band positions of certain 2D TMO&Cs are strongly dependent on their thickness and lateral dimensions [44–49]. In many cases, the CB edge will shift toward H_2 reduction potential or the VB edge will shift toward O_2 oxidation potential or both happen simultaneously [49]. Therefore, the increased thermodynamic driving force is expected according to the Marcus–Gerischer theory [50, 51]. Moreover, the unique 2D layered structure can be a suitable matrix to induce some special optical phenomena such as plasmonic effect that possibly extends the absorption range of solar spectrum [52, 53].

In this review, we aim to summarize and provide critical discussions on current 2D TMO&C-based photocatalysts compared to their bulk and other dimensional counterparts, with particular focuses on their crystal structures, morphologies and electronic band structures. The methods for synthesizing these photocatalysts are also described in brief. In addition, various approaches on improving the photocatalytic performances of 2D TMO&Cs, such as elemental doping, surface functionalization and heterojunction formation, are critically discussed in terms of their fundamentals and fabrication methods. Finally, a summary of current research progress and perspectives on the challenges and future research directions are given.

In addition, we refer to TMO (e.g., MoO_3) and TMC (e.g., MoS_2, $MoSe_2$ and $MoTe_2$) separately on purpose. This distinction is frequently applied throughout the literature, despite oxygen being a member of the chalcogen group. The origin of this arguably non-intuitive definition is associated with the properties of these inorganic compounds. While a metal's sulfide, selenide and telluride compounds frequently feature similar properties, the corresponding oxides exhibit stark different properties and stochiometries. As a result, the more similarly behaving compounds are grouped together as chalcogenides, while oxides, being usually the exception to observed trends, are discussed separately.

2 The Current Deployment of 2D Single Transition Metal Oxides and Chalcogenides in Photocatalytic Applications

Currently, the deployments of 2D TMO&Cs in photocatalytic applications are relatively limited compared to the nanoparticle and 1D nanostructure systems. 2D TMO&Cs can be classified into two major categories in terms of their crystal structure: (1) layered materials which possess strong lateral chemical bonding in planes but exhibit weak van der Waals interaction between planes and (2) non-layered materials which form atomic bonding in three dimensions and their growth is stopped after a finite numbers of layers with the 2D sheetlike structures [54].
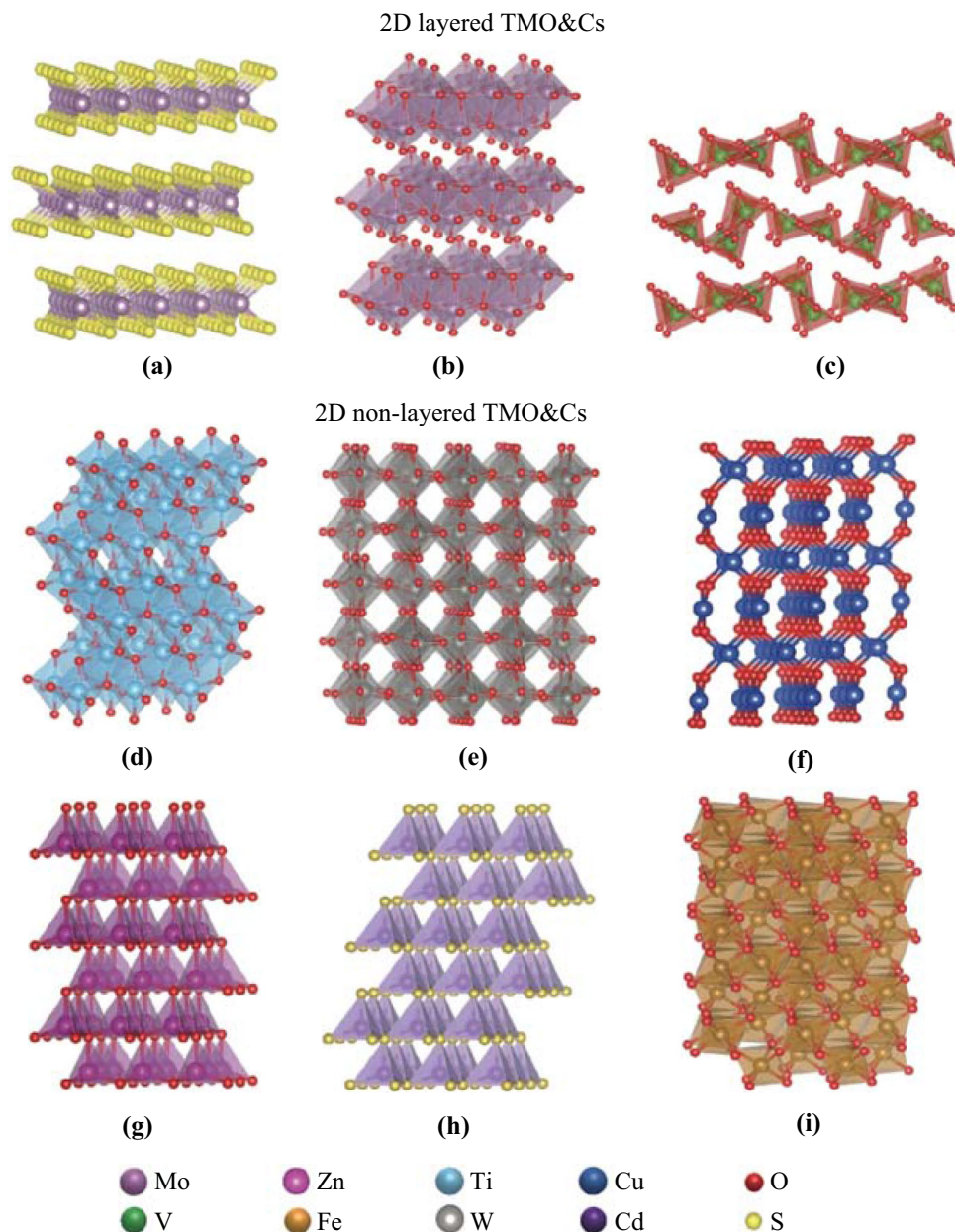
2.1 Layered 2D TMO&Cs

Mo- and W-based chalcogenides (MX_2, M = Mo or W and X = S, Se or Te) are typical layered 2D TMCs and emerging photocatalytic materials [55–57]. MX_2 has a stable hexagonal crystal structure named 2H phase with semiconducting properties. A monolayer of MX_2 generally consists of two planes of hexagonally arranged X atoms linked to a hexagonal plane of M atoms via covalent bonds (Fig. 2a) [58]. Each M atom is prismatically coordinated by six surrounding X atoms [59]. Such a hexagonal crystal structure can be also seen in a large number of TMCs including the sulfide, selenide and telluride compounds with transition metal element from group IV (Ti, Zr, Hf and so on) and group V (V, Nb or Ta) [37].

Interestingly, the stable 2H semiconducting phase can be transformed to a metastable metallic phase called 1T phase through chemical and electrochemical intercalation of alkaline ions [60]. During the transformation, the planar 2D morphology can be normally retained, but the coordination of M atoms in reference to the surrounding X atoms becomes octahedral [61]. Such a transformation activates the catalytic property of the basal plane in the 2D planar

structure, introducing more catalytic sites in the material. Another interesting aspect is that the electronic band structure of MX_2 is gradually changed from indirect to direct and its bandgap energy enlarges concurrently, when the thickness of MX_2 is reduced to monolayer [62]. Their CB edges are found to be shifted above the H_2 reduction potential during the transformation, which implies that its hydrogen evolution reaction (HER) will be more thermodynamically favorable (Fig. 1b). In addition, their bandgap energies lie within the region between 1.6 and 2.4 eV which is ideal for the absorption of visible light. The occurrence of band nesting in their band structures allows highly efficient light absorption at optical gaps other than direct bandgaps, giving rise to absorption as high as 30% at resonance [63]. However, their excited state dynamics studies reveal that the indirect–direct band gap transition in monolayer and few-layer Mo- and W-based TMC results in faster exciton recombination that is dominated by the non-radiative relaxation pathways [64–67], rendering their applications in photocatalysts individually [68]. In addition, the density of surface trap states in monolayer and few-layer structures may affect the trapping of excitons, possibly providing an approach for controlling the exciton dynamics in the 2D systems. Instead, 2D MX_2 is generally coupled with other visible light-driven photocatalyst as a co-catalyst and electron sink [69, 70]. Detailed discussion will be presented in the later section. The lateral dimensions of 2D MX_2 used in the photocatalyst are normally within 5 μm, and their thicknesses are less than 10 layers. In comparison, the photocatalytic properties of other layered 2D TMCs are rarely explored. The Zr-, Hf-, Pd- and Pt-based chalcogenides may merit for further investigation due to their narrow bandgaps and suitable band positions [71].

For 2D layered TMO, the research mainly focuses on MoO_3 and V_2O_5. 2D MoO_3 is generally with the thermodynamically stable orthorhombic phase (α phase). Each individual atomic layer consists of dual-layer planar crystals of distorted MoO_6 octahedra, held together by weak van der Waals forces in the vertical {010} direction (Fig. 2b) [72]. The internal bonds within the octahedra are dominated by covalent bonds instead. Each of the double layers forms edge sharing zigzag rows along the {001} and corner-sharing rows along the {100} directions, respectively. MoO_3 also has a metastable phase named β phase but adopts a monoclinic 3D structure, which is not desirable for forming planar crystals [73]. The photocatalytic performance of 2D α-MoO_3 nanoplatelets with lateral dimension of up to 500 nm and thickness of 20–40 nm is evaluated by Anthony et al. through the degradation of methylene blue (MB) and rhodamine B (RhB) dyes under the irradiation of sunlight. Excellent degradation rates are found to be in the range of 0.8–1.2 mmol $(gh)^{-1}$ [74].

2D layered TMO&Cs

(a)   **(b)**   **(c)**

2D non-layered TMO&Cs

(d)   **(e)**   **(f)**

(g)   **(h)**   **(i)**

Mo   Zn   Ti   Cu   O
V   Fe   W   Cd   S

Fig. 2 Crystal Structure of **a** hexagonal 2H MoS_2, **b** orthorhombic MoO_3, **c** orthorhombic V_2O_5, **d** anatase TiO_2, **e** monoclinic WO_3, **f** monoclinic CuO, **g** wurtzite ZnO, **h** wurtzite CdS, and **i** rhombohedral Fe_2O_3

Similarly, 2D V_2O_5 generally has an orthorhombic crystal structure, consisting of zigzag double chains of square-based VO_5 pyramids, bonded together with corner-shared bridge oxygen atoms (Fig. 2c) [75]. Although the photo-catalytic H_2 production rate of 2D V_2O_5 nanosheets with lateral dimension of ~ 80 nm is relatively low (~ 0.1 mmol $(gh)^{-1}$) due to its unfavorable band position, however, the enhanced surface area in such a 2D system still demonstrates a significant improvement in reference to the commercial powder counterpart (~ 0.03 mmol $(gh)^{-1}$) [76].

2.2 Non-Layered 2D TMO&Cs

In non-layered 2D TMO&Cs, 2D TiO_2 undoubtedly is the most studied candidate for photocatalyst followed by great success achieved by its bulk and nanoparticle systems [77]. Generally, TiO_2 has three most commonly encountered crystalline polymorphs including anatase, brookite and rutile, in which anatase is the most common crystal structure in the 2D configuration [42]. Anatase adopts a tetragonal structure with the share of two opposing edges of each TiO_6 octahedron to form linear chains along the {001} direction (Fig. 2d) [78]. Interestingly, the mixture of

rutile and anatase phases creates a type II band alignment of ~ 0.4 eV, causing the significant decrease in effective bandgap energy and facilitating efficient photoinduced charge separation [79].

It is noted that the particular crystal facet can greatly affect the photocatalytic performance of TiO_2. Both theoretical and experimental studies found that the facets in the equilibrium state are especially reactive [78]. However, for the conventional anatase TiO_2 nanocrystal system, it is dominated by either {101} or {001} facets which are less energetically favorable for catalytic reaction [42]. The 2D planar morphology provides the opportunity to engineer the yield of exposed {001} facet in anatase TiO_2 as large as 95%. In this case, the basal plane of the 2D nanosheet is dominated by the {001} facets on the basis of the symmetries of anatase crystal structure [42]. For the nanosheets with dimension of < 100 nm, it demonstrates a more than four times enhancement in both H_2 and CH_4 evolution rates compared to those of conventional anatase nanocrystals [42]. Furthermore, theoretical calculation showed that the {101} and {001} facets exhibited different band edge positions, possibly resulting in forming a surface heterojunction within single TiO_2 nanosheet and hence facilitating the photogenerated charge separation [43]. When there is Ti deficiency existed in TiO_2, the corresponding crystal structure may be transformed to an orthorhombic system. Such a group of TiO_2 derivatives is generally named as "titanate" [77]. Each titanate layer belongs to the lepidocrocite type that consists of two TiO_6 octahedra connected via edge sharing to form a 2D feature [77]. The bandgap of 2D titanate nanostructure is higher than that of TiO_2, but the resulted higher CB and lower VB edges are advantageous for photocatalytic performances [77]. Nevertheless, one drawback is the use of more powerful UV light to activate the 2D titanate system. Therefore, it is essential to couple with a visible light-driven photocatalyst for practical applications [77]. Details of the heterostructures will be discussed in the later section.

ZnO is also a core member in the non-layered 2D photocatalyst family. In its bulk form, ZnO crystallizes in either hexagonal wurtzite, cubic zinc-blende structure or both at ambient pressure [80]. Most of the reported 2D ZnO nanostructures are dominated by the wurtzite structure [81]. The structure is composed of two interpenetrating hexagonal close-packed sublattices, each of which consists of one type of atom displaced with respect to each other along the {001} direction (Fig. 2g) [82]. However, scanning tunneling microscopic observations in ultrathin ZnO planar nanostructure reveal that the wurtzite structure may be collapsed and subsequently transformed into a specific 2D arrangement [83]. In addition, the detailed discussion on the specific band structure of 2D ZnO in comparison with the bulk counterpart is rarely found at the moment and

further investigation on relevant topics is needed. Both individual 2D nanosheets and 3D hierarchical structures are investigated for their photocatalytic performances toward the degradation of organic dyes [84–86]. The dimension of the structures is generally in the range between 1 and 10 μm and the thickness of individual 2D building block of less than 50 nm. There is generally a one- to two-order enhancement on 2D ZnO regarding the photodegradation performance compared to the nanoparticle system [86].

Similar to ZnO, 2D Zn- and Cd-based chalcogenides also share similar wurtzite crystal structure and have been widely deployed as photocatalysts (Fig. 2h) [87–89]. For example, it is demonstrated that 2D ZnS nanosheets with the lateral dimension of 500 nm exhibit a considerable degradation rate of 0.35 mmol $(gh)^{-1}$ toward methyl orange (MO) under the UV irradiation. It is inactive under visible light exposure due to its large bandgap energy [88]. In comparison, ZnSe has a much narrow bandgap energy of ~ 2.7 eV; hence, it is much popular to be a visible light-driven photocatalyst [90]. 2D ZnSe nanosheets with a lateral dimension of ~ 3 to 5 μm demonstrated a more than 50% enhancement on the RhB degradation rate compared to that of conventional nanoparticle counterpart under visible light illumination [90]. The assembled 3D ZnO hierarchical microspheres also show a MO degradation rate of 40 μmol $(gh)^{-1}$ which is almost 3 times larger than that of nanoparticle system [91]. For the Cd-based 2D chalcogenides, 2D CdS nanosheets with a lateral size of 100–300 nm and a thickness of a few nm demonstrate an excellent H_2 production rate of ~ 41 mmol $(gh)^{-1}$ under visible light irradiation [92]. Under similar experimental conditions, its 3D flower-shaped derivative with lateral dimension of 300–800 nm also shows an enhanced H_2 production rate of ~ 9 mmol $(gh)^{-1}$ which is almost 3 times higher than that of nanoparticle system [93]. The H_2 production rate of flowerlike CdSe ultrathin nanosheet assemblies is more than threefold compared to the commercial powder counterpart. Such an impressive improvement can be ascribed to its enhanced surface area as well as the shift of CB edge above the H_2/H_2O potential possibly due to the quantum confinement effect [48].

WO_3 is another popular non-layered 2D candidate. Monoclinic phase is the most common crystal structure in 2D WO_3, which contains oxygen corner-sharing WO_6 octahedrons in a slightly distorted cubic arrangement (Fig. 2e) [94]. Chen et al. propose that the bandgap of the 2D nanosheet (lateral dimension of 1–2 μm and thickness of ~ 9 nm) is slightly larger than the bulk crystal with the positive shift of both CB and VB edges. Therefore, these 2D WO_3 nanosheets can become an efficient photocatalyst for evaluating CH_4 at a rate of 1.5 μmol $(gh)^{-1}$ [49]. The 2D WO_3 nanoplatelets with the lateral dimension of

$\sim$ 200 nm also demonstrate a RhB photocatalytic degradation rate of $\sim$ 1 mmol (gh)$^{-1}$ compared to $\sim$ 0.4 mmol (gh)$^{-1}$ of commercial powder [95]. Its 3D flower-shaped assembled structures with average dimension of 1 μm even show a much enhanced photodegradation performance ($\sim$ 1.3 mmol (gh)$^{-1}$) [96]. Similar enhancement factor ($\sim$ 2.6 mmol (gh)$^{-1}$) is also observed in the slightly hydrated 3D WO$_3$ flower-shaped structure [97].

Other non-layered 2D TMO&Cs such as α-Fe$_2$O$_3$ and CuO are also studied for their photocatalytic properties but to a less extent [98, 99]. α-Fe$_2$O$_3$ commonly has a rhombohedral structure consisting of FeO$_6$ octahedra that share edges with three neighboring octahedra in the same plane and one face with an octahedron in an adjacent plane in the {001} direction (Fig. 2i) [100]. The photocatalytic performance of individual 2D α-Fe$_2$O$_3$ nanostructure is rarely found in the literature. Instead, the 3D hierarchical nanostructure such as hollow spheres assembled by 2D nanosheets (average dimension of 70 nm) demonstrates the capability of photocatalytic salicylic acid degradation under UV light exposure at a rate of 176 mmol (gh)$^{-1}$, which is more than 40% enhancement than that of nanoparticle [101]. For 2D CuO, the crystal structure belongs to the monoclinic system, in which the Cu atom is coordinated by four coplanar O atoms forming an almost rectangular parallelogram, while the O coordination polyhedron has four Cu atoms at the corners of a distorted tetrahedron (Fig. 2f) [102]. The bandgap of 2D CuO nanosheets (lateral dimension of $\sim$ 1 μm and thickness of < 10 nm) is measured to be $\sim$ 2.0 eV which is much larger than the bulk ($\sim$ 1.4 eV) (Fig. 1). Such a bandgap enlargement can be again ascribed to both the quantum size effect and the domination of (002) exposed facet in the 2D configuration [103]. The photodegradation rate of MO under the UV light exposure is 45.5 μmol (gh)$^{-1}$ which is double than that of nanoparticle counterpart [103].

2.3 Synthesis Techniques of 2D TMO&Cs for Photocatalysts

As the material loading plays an important role in photocatalytic performances, some conventional synthesis approaches for 2D TMO&Cs, such as mechanical exfoliation technique, are not practical to use due to their low production yield (Fig. 3). Chemical vapor deposition (CVD) technique is potentially a suitable candidate for mass production although it is currently not commonly used for preparing 2D photocatalysts. Chemical intercalation (Fig. 4a) and sonication-based (Fig. 4b) liquid-phase exfoliation techniques are generally deployed in 2D layered TMO&C photocatalysts including the most studied MoS$_2$ and WS$_2$ [104]. Liquid-phase exfoliation technique can also be applied in non-layered 2D TMO&Cs. Taking
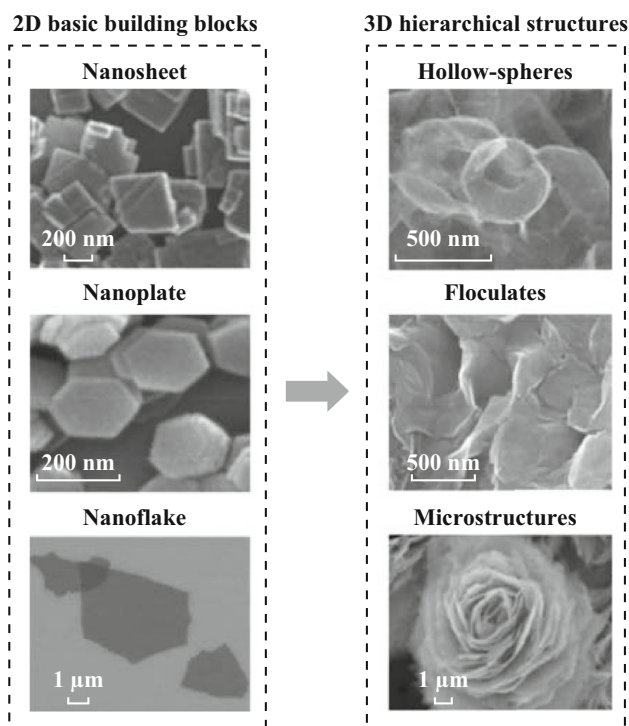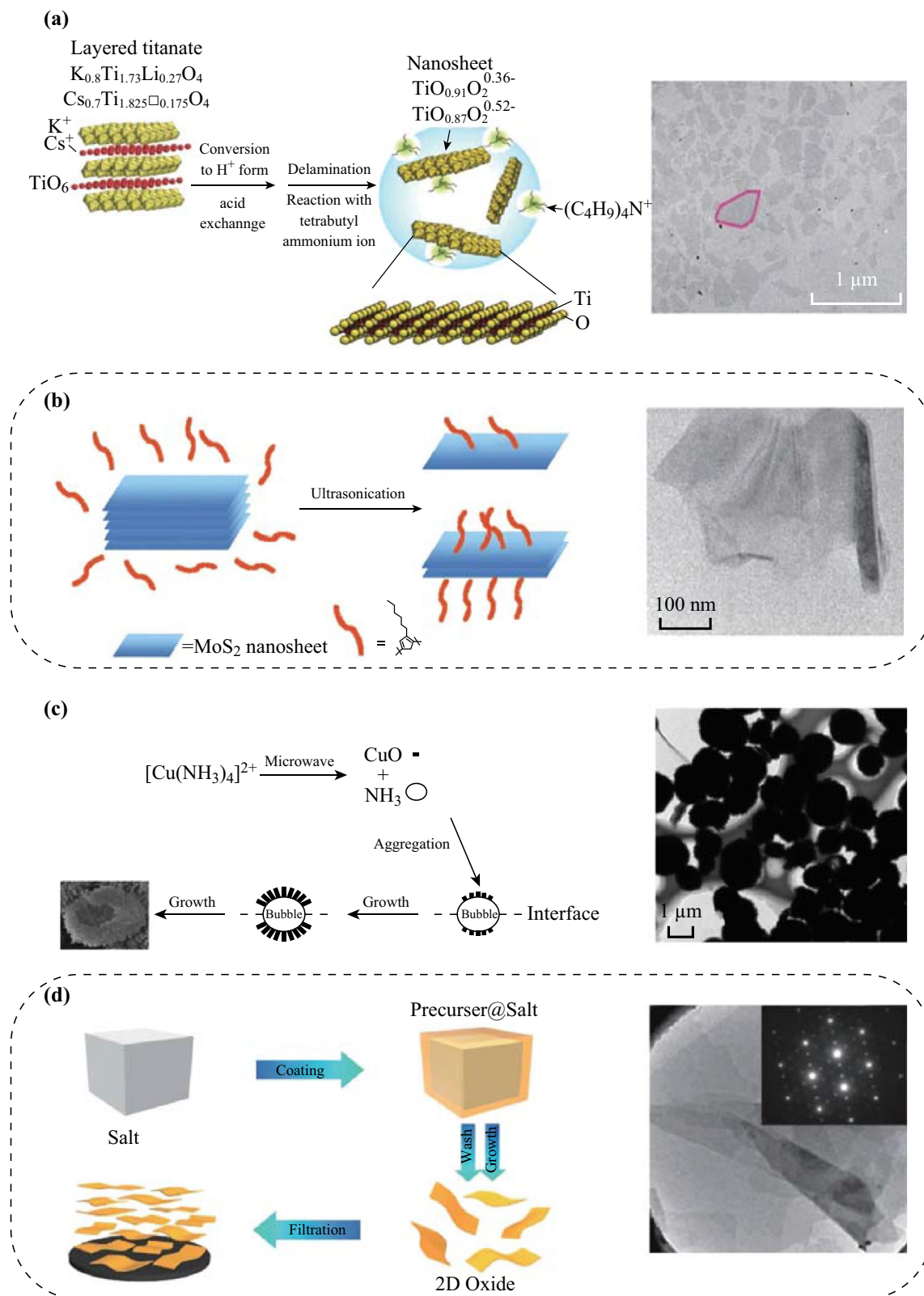

Fig. 3 Representative scanning electron microscopic images of the 2D basic building blocks and common 3D hierarchical structures. Reproduced with the permission from Ref. [84, 98, 122, 151, 169, 211]

the example of 2D titanate (e.g., Ti$_{0.91}$O$_2$) nanosheets, layered protonated titanate (e.g., H$_{0.68}$Ti$_{1.83}$O$_4$·H$_2$O) is chosen as the start material due to the non-layered nature of anatase TiO$_2$ [105]. The interlayer of the protonated titanate is significantly expanded by replacing the protons with bulky organic ions such as tetra-butylammonium ions (TBA$^+$) [105], hence enabling the exfoliation process by applying a weak shear force in the liquid solution [105]. Similarly, 2D WO$_3$ nanosheets are obtained from layered tungstate (e.g., WO$_3$·2H$_2$O) [106].

The 2D nanostructures can also be obtained hydrothermally/solvothermally using specific precursors for chemical reaction in a pressurized autoclave at elevated temperatures (Fig. 5a) [42, 43, 96, 97]. For example, 2D MoS$_2$ nanosheets are synthesized using MoO$_3$ and potassium thiocyanate (KSCN) mixture as the source of Mo and S, respectively [107]. For the production of 2D MoO$_3$ nanosheets, the precursor consisting of molybdate salt and organic aliphatic acids is used for hydrothermal synthesis [74]. Special attention should be paid to select appropriate reducing agent as unintentional elemental doping may occur in the resulted TMO&Cs.

In addition to the individual 2D nanostructures, functional architectures can be assembled with 2D building

(a)

Layered titanate
$K_{0.8}Ti_{1.73}Li_{0.27}O_4$
$Cs_{0.7}Ti_{1.825}\square_{0.175}O_4$

K^+
Cs^+

TiO_6

Conversion to H^+ form
acid exchannge

Delamination
Reaction with tetrabutyl ammonium ion

Nanosheet
$TiO_{0.91}O_2^{0.36-}$
$TiO_{0.87}O_2^{0.52-}$

$(C_4H_9)_4N^+$

Ti
O

1 μm

(b)

Ultrasonication

= MoS₂ nanosheet   =

100 nm

(c)

$[Cu(NH_3)_4]^{2+}$ Microwave CuO
+
NH_3

Aggregation

Growth   Growth

Bubble   Bubble   Interface

1 μm

(d)

Salt

Coating

Precurser@Salt

Wash
Growth

2D Oxide

Filtration

Fig. 4 Schematics of synthesis procedures of **a** chemical intercalation, **b** sonication assisted, **c** microwave assisted **d** template assisted for producing 2D TMO&C-based photocatalysts and the corresponding transmission electron microscopic images. Reproduced with permission from Ref. [77, 99, 212, 213]

(a) Hydrothermal 2D nanosheet

(b) Hydrothermal 3D structure
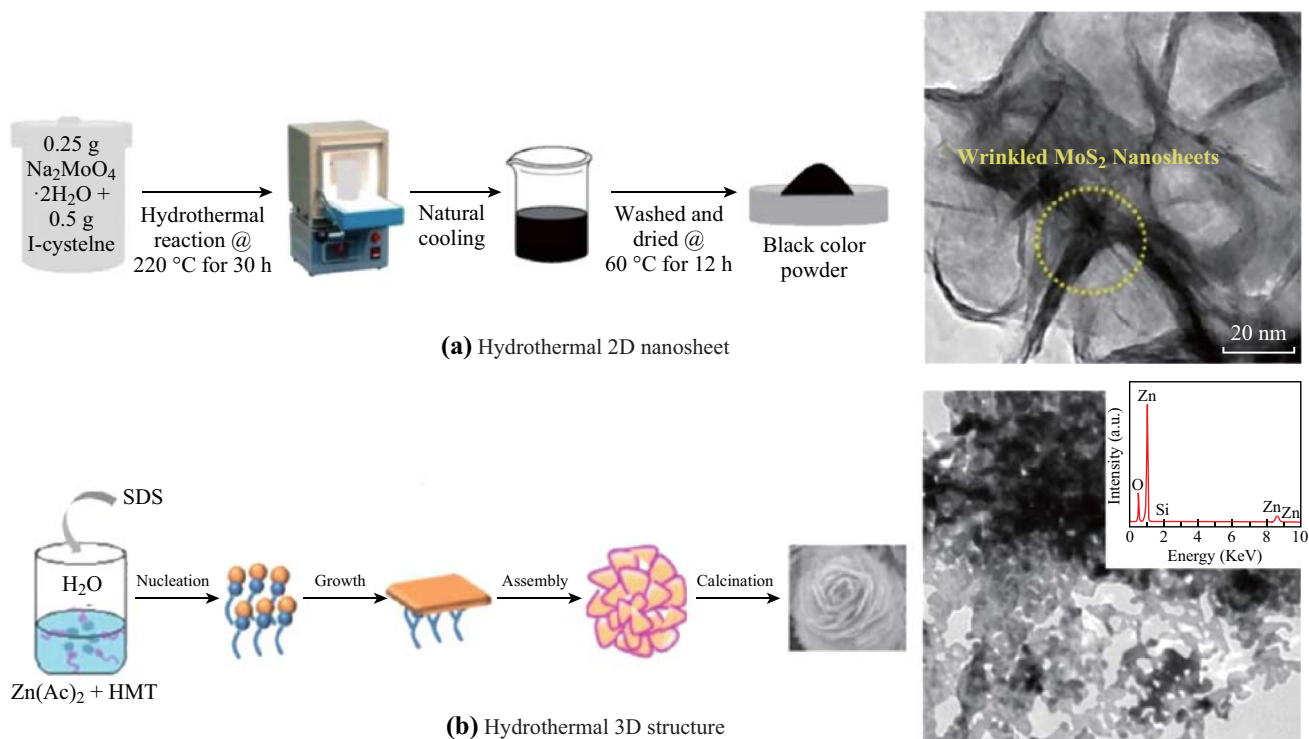
Fig. 5 Schematics of hydrothermal synthesis procedures of **a** individual 2D nanostructures and **b** 3D hierarchically assembled structures and their corresponding transmission electron microscopic images. Reproduced with permission from Ref. [84, 214]

blocks using the hydrothermal/solvothermal technique, which are also considered as an important member in 2D TMO&C-based photocatalyst (Fig. 3) [55, 62, 76]. These three-dimensional (3D) assembled structures can significantly improve the photocatalytic performance due to their enhanced active surface area and increased photon–matter interaction via multiple reflection and scattering at the catalyst–electrolyte interface [108]. The selection of capping agent is important for directing the growth of 3D TMO&Cs (Fig. 5b). For example, the selection of thiourea, thioamide or thioacetamide as the chalcogenide during the synthesis results in the 3D MoS_2 hierarchical structures in the forms of microspheres, ordered flocculates or flowers [62], respectively. The introduction of citric acid as a capping agent facilitates the crystal growth of ZnO along {001} orientation, leading to the formation of 2D nanosheets or 3D hierarchical micro-flowers. However, the absence of citric acid leads to the formation of 1D needlelike morphology due to significant etching along the {001} direction by KOH as a co-reaction agent [109]. The selection of solvent is another important factor to influence the structural and morphological properties of 2D TMO&Cs. Zhang et al. [110] demonstrate that the increase in volume ratio between ethylenediamine and ethylene glycol in the solvent composition transforms the ZnO from the 1D rodlike structures to 3D spherical nano-flowers. Other factors such as temperature and experiment duration

are also reported to affect the crystal nucleation behaviors, therefore enabling the precise control of the morphologies and crystallinity of 2D TMO&Cs and their 3D derivative hierarchical structures [111].

It is also reported that high-temperature calcination of TMC can effectively produce 2D TMOs [112]. The application of microwave radiation (Fig. 4c), aqueous-soluble salt templates (Fig. 4d), UV light exposure and electrical field can assist the synthesis of non-layered 2D TMO&C nanostructures including Fe_2O_3, WO_3, CuO and ZnS [49, 88, 99, 101]. Other methods including pyrolysis of metal salts, hot chemical bath and sol–gel have been demonstrated to produce 3D TMO&C hierarchical structures [76].

3 Improvement Approach of Photocatalytic Performances in 2D Transition Metal Oxides and Chalcogenides

3.1 Elemental Doping

Elemental doping is a conventional and effective approach to modify the surface properties and band structures of bulk TMO&Cs for efficient visible light harvesting and enhancement of redox activities [6]. The possible increased mechanical flexibility in some 2D TMO&Cs may result in
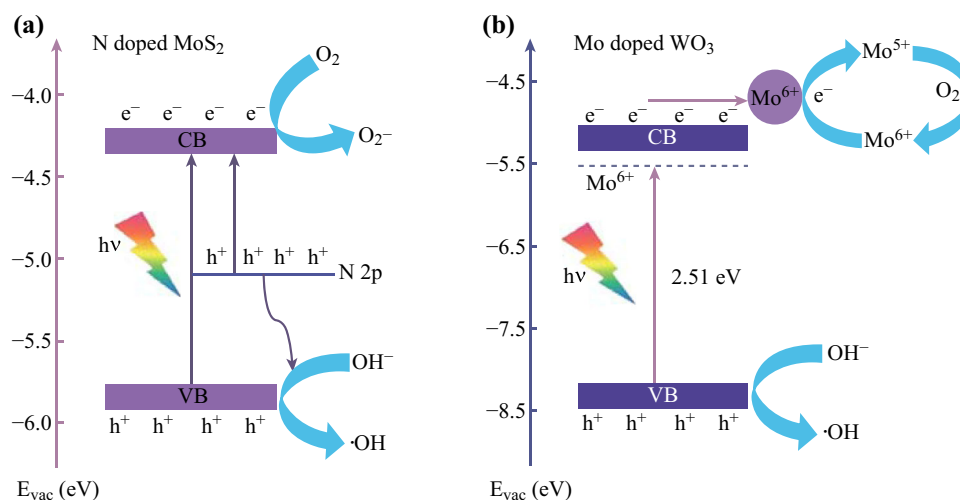
Fig. 6 Influence of elemental doping of **a** nonmetal element (N-doped MoS_2 nanosheets) and **b** metal element (Mo doped WO_3 nanosheets) toward the band structure. Reproduced with permission from Ref. [117, 122]

better incorporation of size-mismatched dopant ions in the crystal compared to the bulk counterpart [113]. The dopants can be generally classified into metal and nonmetal elements [6]. Upon doping with nonmetal elements, the bandgap of TMO&Cs is normally narrowed due to the overlapping between the orbitals of dopant and oxygen/chalcogenide atom [114]. It is also proposed that the formation of localized states within the bandgap by the dopant can contribute to the bandgap narrowing [115]. In this case, the photogenerated electrons can be directly excited from the dopant gap state, instead of the VB edge, to the CB of the material (Fig. 6a). For metal doping, the ionic radius and valence state of the dopant, in reference to those of host metal cation, both play an important role in the determination of occupied sites and electronic properties of the dopant. They may influence the surface properties, position of the Fermi level as well as the conductivity within the matrix [116]. Regardless, the interaction of the dopant with the host lattice leads to the formation of new energy levels either within or beyond the bandgap of TMO&Cs [116]. The light absorption edge can hence be redshifted by electronic transitions from the VB and/or to the CB (Fig. 6). Both metal and nonmetal dopants can also facilitate the separation of photogenerated charge carriers. In particular, when at appropriate concentrations, the dopants can act as deep trap sites for one type of charge carrier, while allowing another one to reach the material surface for desired redox reactions [6].

Nonmetal elements such as N, B, F, P and C have so far been investigated for doping the 2D TMO&Cs. The doping process is mainly realized through the pre-treatment of precursors for synthesis, and the resulted dopant concentration is low which generally causes minimum distortions

to the host crystal structure. For example, Liu et al. synthesize the N-doped MoS_2 hierarchical flower-shaped structure using a sol–gel method, in which thiourea $((NH_2)_2CS)$ is used for the nitrogen dopant source. The bandgap energy of N-doped MoS_2 (2.08 eV) is slightly lower than those of MoS_2 nanosheets (2.17 eV), which can be ascribed to the formation of defect state by N dopants in the bandgap of MoS_2 (Fig. 4a). As a result, the N dopant in MoS_2 activates its photocatalytic properties, in which the RhB dye is photodegraded in a rate of 134 μmol $(gh)^{-1}$, while no performance is reported in 2D MoS_2 nanosheets [117].

Similarly, N-doped 2D TiO_2 nanosheets are produced by a conventional hydrothermal synthesis approach using nitric acid (HNO_3) as the N dopant source. They have an enhanced visible light absorption in the range from 380 to 500 nm. In addition, the accommodation of N dopants in the TiO_2 crystal structure favorably enhances the number of exposed {001} facets, which are considered as the highly active catalytic site for TiO_2 [42, 118]. The resulting H_2 production rate for the N-doped nanosheets is as high as 17.2 mmol $(gh)^{-1}$, which is about four and two times higher than those of N-doped microcrystals and 2D bare nanosheets, respectively [42, 118]. The selection of tetrafluoroboric acid (HBF_4) as the hydrothermal reaction agent during the synthesis results in the co-doping of B and F in 2D TiO_2 nanosheets, which are also dominated by the {001} exposed facets and have a visible light absorption edge appeared at around 516 nm [119].

For 2D ZnO, the introduction of C self-dopants during the hydrothermal synthesis creates a new gap state at the top of the VB and several states mixed with the CB edge, extending the absorption edge to up to 430 nm. The RhB

photodegradation rate of the C-doped ZnO is 1.5 μmol $(gh)^{-1}$ that is four times larger than that of commercial powder [120]. However, for P-doped 2D ZnO nanosheets, the bandgap narrowing effect is less obvious. Instead, the dopants play a critical role in obtaining such a 2D planar nanostructure [121].

In comparison, the metal doping is a relatively less common approach for the bandgap engineering of 2D TMO&C structures. Li et al. synthesize the 2D WO_3 nanosheet doped with Mo ions using ammonium molybdate as the dopant source (Fig. 8a, b). As the ionic radius of Mo is close to that of W, Mo ions are incorporated into the W lattice without disturbing the monoclinic crystal structure. Mo doping created a donor level under the conduction band of WO_3 to increase the absorption intensity of visible light. The bandgap of Mo-doped 2D WO_3 decreases from 2.56 to 2.36 eV with the increase in Mo atom (Fig. 6b) content from 0.5 to 10%, The corresponding RhB photodegradation performance is increased from 8 to 12.5 μmol $(gh)^{-1}$ [122]. In comparison, the Mn dopants in 2D CuO nanosheet decrease the host lattice parameters due to the additional strain in the crystal lattice given by different ionic radii between Cu^{2+} and Mn^{2+}. 6 wt% of Mn dopant causes a significant reduction in the CuO bandgap energy down to $\sim$ 1.25 eV, resulting in a broad absorption in the region of 200–800 nm. The corresponding photocatalytic MB degradation rate for 2D Mn-doped CuO sheets is almost double in comparison with that of bare CuO powder [123].

In addition to the elemental doping, the incorporation of oxygen vacancies in TMOs also alters the bandgap energy through the formation of localized defect states within the bandgap. The electrical conductivity is improved at the same time, which potentially reduces the charge recombination rate [124]. Furthermore, the partial reduction in the metal oxidation state can act as the trap of electron, hence facilitating the photogenerated charge separation [124]. Certain 2D TMO&Cs can potentially accommodate a large number of oxygen/chalcogen vacancies, significantly increasing the free charge carrier concentration up to $\sim 10^{21}$ cm^{-3} and simultaneously transforming the material from semiconducting to quasi-metallic [125]. Surface plasmon resonance is therefore induced in either the visible or near-infrared spectrum, which greatly improves the solar light harvesting performance of the material [53]. Some pioneer works on standalone 2D MoO_{3-x} nanosheets and core–shell structured 2D MoO_{3-x}/MoO_3 nanosheets have shown improved visible light absorption and demonstrated significantly enhanced photocatalytic performances compared to those of stoichiometric counterpart [126, 127].

3.2 Surface Functionalization

Depending on the specific type of photocatalytic application, functionalization of 2D TMO&Cs with a particular organic group can potentially adsorb more surface species and hence improve the photocatalytic performances. Xue et al. functionalize 2D ZnO nanosheets with amine to enhance the surface capture of CO_2 molecules for photocatalytic CO_2 reduction. Monoethanolamine (MEA) is utilized to possess a hydroxyl group for covalent attachment on ZnO and a primary amine group to endow an amine-functionalized surface. The efficient creation of C–N bonding with CO_2 in the terminal amine groups is believed to activate CO_2 and produce carbamate. The presence of carbamate can establish direct interactions with Zn^{2+} to receive electrons from ZnO and implement reduction reactions toward CO and CH_4. From the experiment, both the CO and CH_4 production rates exhibited by amine-functionalized ZnO nanosheets are double compared to those of bare counterpart [128].

In addition, being aspired by dye-sensitized solar cells, the sensitization of dye molecules on the semiconductor surface is an emerging approach to enhance visible light harvesting [129, 130]. When incorporated into 2D TMO&C systems, the amount of adsorbed dyes can be superior due to the ultra-large surface area offered by the 2D planar geometry [131]. Among various dyes, noble metal-free zinc porphyrin complexes have been studied intensively as photosensitizers for dye-sensitized solar cells with their highest conversion efficiency of $> 10\%$ [132]. Due to the delocalized p electrons, zinc porphyrin has strong absorption in visible light region, outstanding photochemical stability and more importantly, suitable redox potentials for electron injection and dye regeneration, making it attractive as photosensitizers [133]. In a few recent reports, zinc porphyrin has been incorporated into the 2D MoS_2 nanosheet heterostructured with TiO_2 and ZnO [131, 133]. In this system, the electrons are excited from the highest occupied molecular orbital (HOMO) to the lowest unoccupied molecular orbital (LUMO) of zinc porphyrin complexes to form an excited intermediate upon visible light illumination (Fig. 7). Due to the relatively negative oxidation potential of the dye, the generated electrons are injected from the excited zinc porphyrin complexes to TMO. Then, 2D MoS_2 nanosheet is utilized as a co-catalyst, which collects the excited electrons from the TMO for HER. The enhancement factor of photocatalytic H_2 production when incorporated porphyrin complexes can exceed one order compared to the bare $MoS_2/$ TMO heterostructure [131, 133]. In addition to zinc porphyrin complexes, eosin Y is also utilized in 2D MoS_2 nanosheet–graphene composites [134]. Although superior photocatalytic hydrogen evolution is demonstrated, the

longevity of this dye-functionalized photocatalytic system may be questioned due to the short lifetime of the dye.

3.3 Heterojunctions

#### 3.3.1 Heterojunction with Semiconductors

In addition to the limited visible light harvesting performance, fast recombination of photogenerated charge carrier in many individual 2D TMO&Cs is a great concern. Constructing a 2D TMO&C-based heterojunction with a properly selected semiconductor can address such a concern [6]. A good matching of CB and VB energetic levels
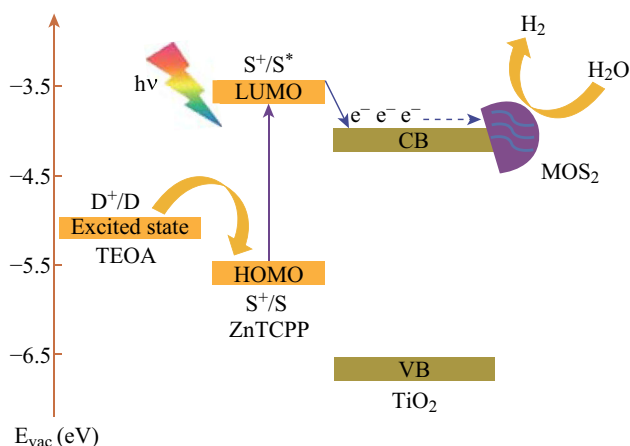
Fig. 7 Influence of zinc porphyrin functionalization on the surface of TiO_2/MoS_2 in terms of electronic band structure. Reproduced with permission from Ref. [131]

between 2D TMO&Cs and the semiconductor can produce an effective transfer pathway for photogenerated charge carriers from one to the other. The most popular approach is the type II band alignment (Fig. 9b). The photogenerated electrons transfer from the more positive CB edge to the less positive one, while the holes transfer from the more negative VB edge to the less negative one, hence realizing the spatial charge carrier separation [135]. However, many other factors, such as defect density and crystallinity, can significantly alter the band structures of the materials hence influencing the coupling efficiency [6]. Furthermore, the dimensionality and size difference between coupled semiconductors may also be important for hetero-interfacial contacts [108]. Compared to other 2D/low-dimensional counterparts, the 2D/2D heterostructure (Fig. 8g, h) exhibits better stability and coupling heterointerfaces due to the large contact surface and short exciton diffusion length in the contact, which facilitates the transfer and separation of photoexciton pairs [108].

However, the investigation on 2D/2D semiconducting heterojunctions with type II band alignment is still relatively limited. Most attention has so far been paid to 2D MoS_2-based heterojunctions due to its high electron mobility and excellent electrocatalytic HER performance. Graphic carbon nitride (g-C_3N_4) is a popular 2D semiconductor that forms heterojunction with 2D MoS_2 due to its optimum bandgap energy (2.7 eV) for visible light harvesting as well as proper CB and VB positions for efficient water splitting [136]. In comparison with 2D MoS_2, the CB edge potential of g-C_3N_4 is − 2.8 V (vs. vacuum) which is less negative than that of MoS_2
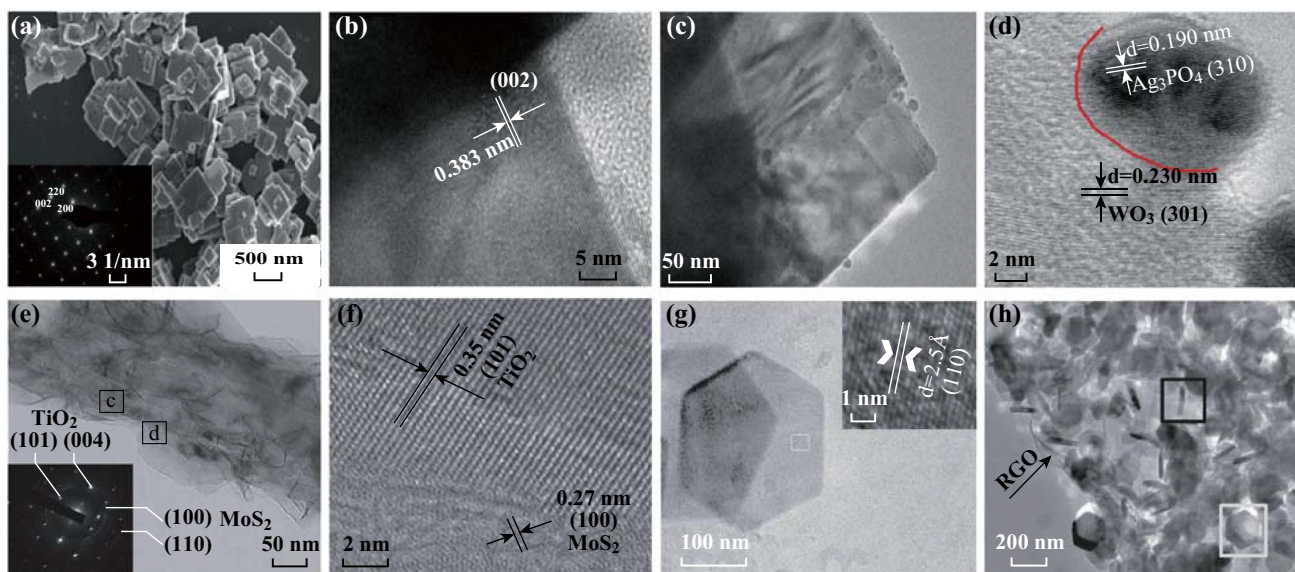
Fig. 8 Representative low- and high-resolution transmission electron microscopic images of **a, b** 2D-doped TMO&C nanosheets, **c, d** 2D–0D heterojunctions, **e, f** 2D–1D heterojunctions and **g, h** 2D–2D heterojunctions. Reproduced with permission from Ref. [56, 98, 122, 168]
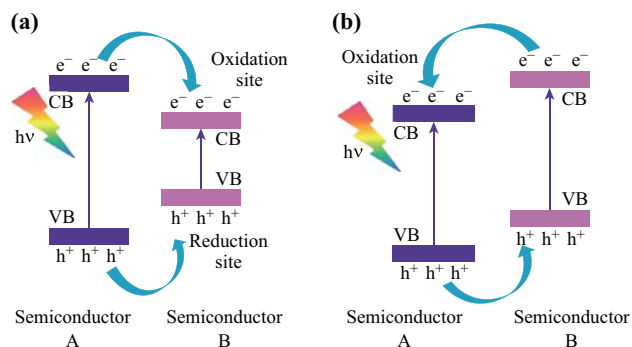
Fig. 9 Semiconducting heterojunctions with **a** type I and **b** type II band alignments. Reproduced with permission from Ref. [215]

($-$ 4.2 V), allowing the migration of electrons from g-C_3N_4 to MoS_2. On the other hand, the hole generated from MoS_2 can be transferred to g-C_3N_4 due to more negative VB potential of MoS_2 ($-$ 6 V) compared to g-C_3N_4 ($-$ 5.5 V), hence achieving efficient charge separation. Therefore, the drawbacks of individual g-C_3N_4-based photocatalyst, such as limited delocalized conductivity and high charge recombination rate, can be significantly alleviated when forming the heterojunction with 2D MoS_2 [55]. In addition, due to the broad visible-NIR absorption range of 2D MoS_2, the heterojunction may have enhanced absorbability of solar light spectrum. The corresponding H_2 evolution rate of g-C_3N_4 loaded with 1 wt% 2D MoS_2 nanosheets is 35.6 μmol (gh)$^{-1}$ which is one order higher than that of g-C_3N_4 [136]. There are also a three times and 20% enhancement on photocatalytic RhB and MO degradation for 2D g-C_3N_4/MoS_2 compared to g-C_3N_4, respectively [55, 137].

2D ZnO nanosheet is another candidate to form 2D/2D semiconducting heterojunction with 2D MoS_2 [138]. While their coupled band structure is identified as type II band alignment by some researchers, it should be noted that the potentials between their CB edges are very close ($-$ 4.4 V for ZnO vs. $-$ 4.2 for MoS_2) [121, 138]. This implies that attention should be paid during the synthesis of 2D ZnO/MoS_2 as minor modifications of the surface may alter the CB edges and hence lead to the transformation to type I

band alignment, which is less favorable for charge separation (Fig. 9a). Furthermore, the CB edge potential of 2D MoS_2 strongly depends on its thickness [139]. Therefore, the influence of 2D MoS_2 thickness in the heterojunction on photocatalytic performances may merit for further investigation. In addition to single TMO&Cs for constructing 2D/2D heterojunctions, binary 2D TMO&C compounds, including $CuInS_4$ and $ZnInS_4$, have also been investigated owing to their relatively narrow bandgap (1.5–1.9 eV for $CuInS_4$ and 2.4–2.5 eV for $ZnInS_4$) and suitable band structures when coupling with 2D MoS_2 [140, 141]. It is found that a loading of 2 wt% 2D MoS_2 in $CuInS_2$-based heterojunction leads to a H_2 evolution rate of 316 μmol (gh)$^{-1}$, which is two order higher than $CuInS_2$ and three times larger than Pt-loaded $CuInS_2$ [141]. Similarly, a double enhancement on the H_2 production rate is observed in the 3 wt% 2D MoS_2/$ZnInS_4$ heterojunction in reference to Pt-loaded $ZnInS_4$ [140].

The heterojunctions of 2D MoS_2 with other low-dimensional TMO&Cs have also been widely investigated. Popular candidates include TiO_2 [56, 69, 70, 142, 143], CdS [144, 145], ZnS [146], MoO_3 [112], ZnO [147] and CuS [148]. The detailed photocatalytic performances are shown in Tables 1, 2, 3, 4, 5 and 6. In these systems, 2D MoS_2 nanosheet is considered as an electron sink candidate similar to the role of graphene, for achieving efficient charge separation in the heterojunction [148]. However, in the view of their band structures, type I band alignment instead of type II is generally achieved in these heterojunctions. The VB edge potential of MoS_2 is less negative than those of aforementioned coupled materials although its CB edge potential is more negative (Fig. 9). Such a band mismatch is less favorable for charge separation as the photogenerated electron–hole pairs from the coupled materials are both transferred to MoS_2. The replacement with metallic 1T MoS_2 may be a viable solution, and its detailed mechanism will be discussed in the later section.

For other 2D TMO&Cs instead of MoS_2, there are also occasional reports on 2D/2D semiconducting heterojunctions with type II band alignment, including 2D g-C_3N_4 coupled with 2D TiO_2 and WS_2 nanosheets [149, 150].

Table 1 Summary of photocatalytic H_2 evolution performance of 2D bare TMO&Cs

Material	Dimension/thickness	Light source	Reaction solution	H_2 PR [% mmol (gh)$^{-1}$]	Comparison	Ref.
TiO_2 NS	70 nm/2 nm	Xe lamp	Methanol	6	1.3 (TiO_2 Cuboids)	[42]
V_2O_5 NS	–	Xe lamp	Methanol	0.022	–	[76]
CdS NS	100–300 nm/4 nm	Visible light	Na_2S/Na_2SO_3	41.1	–	[92]
CdS flower	5 μm/10–100 nm	Xe lamp	Lactic acid and water	9.3	2.6 (CdS NS)	[93]
CdSe flower	5 μm/4.8 nm	Visible light	Na_2S/Na_2SO_3	56.4	0.075 (CdS NR); 44 (CdS QD)	[48]

PR production rate, *NS* nanosheet, *NR* nanorod, *QD* quantum dot

Table 2 Summary of photocatalytic H_2 evolution performance of 2D modified TMO&Cs

Material	Dimension/thickness	Light source	Loading	Reaction solution	H_2 PR (% mmol $(gh)^{-1}$)	Comparison	Ref.
Elemental doping							
N-TiO$_2$ NS	80 nm/20 nm	UV–Vis light	NA	Ethanol	0.865	0.211 (N-TiO$_2$ MC)	[118]
Heterojunction with semiconductors							
TiO$_2$ NS/MoS$_2$ NS	100 nm/12 nm	Xe lamp	0.5 wt% MoS$_2$	Methanol	2.145	0.061 (TiO$_2$)	[193]
MoS$_2$ NS/CdS NP	–	Xe lamp	0.2 wt% MoS$_2$	Lactic acid	5.3	–	[194]
1T-MoS$_2$ NS/TiO$_2$ NC	–	UV light	–	Methanol	2	0.6 (2H-MoS$_2$)	[188]
MoS$_2$ NS/ZnO NP	30–50 nm/–	Xe lamp	1 wt% MoS$_2$	Na$_2$S/Na$_2$SO$_3$	0.765	0.052 (ZnO)	[147]
MoS$_2$ NS/CuInS$_2$ NP	4 μm/80 nm	Xe lamp	3 wt% MoS$_2$	Na$_2$S/Na$_2$SO$_3$	0.316	0.011 (CuInS$_2$)	[141]
MoS$_2$ NS/TiO$_2$ NF	–	Xe lamp	60 wt% MoS$_2$	Na$_2$S/Na$_2$SO$_3$	1.6	–	[142]
MoS$_2$/TiO$_2$ NW	–	Visible light		TEOA-H$_2$O	16.7	–	[70]
1T-WS$_2$/TiO$_2$ NP	100 nm/–	Xe lamp		Distilled water and Methanol	2.57	0.225 (2H-WS$_2$/0D TiO$_2$)	[55]
ZnS/CuS NP	20 nm/–	Visible light		Na$_2$S/Na$_2$SO$_3$	4.147	–	[164]
TiO$_2$ NS/CdS QD	–/0.7 nm	Visible light		Na$_2$S/Na$_2$SO$_3$	0.1	–	[153]
MoS$_2$/N-rGO NS	80 nm/–	Visible light		Ethanol	0.025	–	[162]
Heterojunction with conductive materials							
TiO$_2$ NS/Au–Pd NP	200 nm/–	UV–Vis light	0.3 wt% TiO$_2$	Methanol	0.526	–	[177]
ZnO NS/Au/CdS NP	5 μm/100 nm	W lamp	–	Na$_2$S/Na$_2$SO$_3$	0.608	–	[165]
MoS$_2$ NS/Ag NP	–	Xe lamp	20 wt% MoS$_2$	Na$_2$S/Na$_2$SO$_3$	36	24 (MoS$_2$)	[175]
MoS$_2$-Graphene NS/TiO$_2$ NC	7–10 nm/–	UV light	–	Ethanol/water	2.06	0.0625 (TiO$_2$ NC)	[69]
MoS$_2$-graphene NS/ZnS NP	–	Xe lamp	2 at % MoS$_2$	Na$_2$S/Na$_2$SO$_3$	2.26	0.12 (ZnS)	[146]
MoS$_2$ NS/g-C$_3$N$_4$ NS	–	Xe lamp	0.5 wt% MoS$_2$	Methanol	17.8	–	[136]
WS$_2$ NS/g-CN NS	–	Xe lamp	0.3 at % WS$_2$	Lactic acid	0.12	–	[150]
ZnS NS/Ag$_2$S NP	–/20 nm	Xe lamp	–	Na$_2$S/Na$_2$SO$_3$	0.105	–	[192]
Surface functionalization							
MoS$_2$ NS/ZnTCPP/ZnO NS	–	Visible light	0.5 wt% MoS$_2$	Triethanolamine	0.750	–	[133]
MoS$_2$ NS/ZnTCPP/TiO$_2$ NP	–	Xe lamp	1 wt% MoS$_2$	TEOA	0.102	–	[131]

PR production rate, *NS* nanosheet, *NP* nanoparticle, *NF* nanofiber, *NW* nanowire, *QD* quantum dot, *MC* microcrystal, *NC* nanocrystal

Table 3 Summary of carbon reduction performances of 2D TMO&Cs and their composites

Material	Dimension/thickness	Light source	Reaction solution	Hydrocarbon PR (μmol (gh)$^{-1}$)	Ref.
Single2D TMO&Cs					
WO$_3$ NS	9 nm/4–5 nm	Xe lamp	Distilled water	1.5 (CH$_4$)	[49]
TiO$_2$ NS	80 nm/30 nm	–	Deionised water	1.35 (CH$_4$)	[43]
TiO$_2$ NS	70 nm/2 nm	UV light	Deionised water	5.8 (CH$_4$)	[42]
Heterojunction with semiconductors					
Ti$_{0.91}$O$_2$ NS/CdS NP	–/0.75 nm	Visible light	Deionised water	10 (CH$_4$)	[169]
Heterojunction with conductive materials					
TiO$_2$ NS/r-GO NS	0.1–1 μm/0.75 nm	Visible light	Deionised water	1.14 (CH$_4$); 8.91 (CO)	[187]
Surface functionalization					
Amine–ZnO flower	–	UV light	Ultrapure water	1.1 (CH$_4$); 6.33 (CO)	[128]

PR production rate, *NS* nanosheet, *NP* nanoparticle

Table 4 Summary of pollutant degradation performances of 2D bare TMO&Cs

Material	Dimension/thickness	Light source	Reaction solution	DR (% μmol (gh)$^{-1}$)	Comparison	Ref.
WO$_3$ flower	3–5 μm/25 nm	Xe lamp	RhB	1.3	–	[96]
WO$_{3-x}$/WO$_3$·H$_2$O NW	–	Visible light	MB	70.3	–	[124]
WO$_3$·0.33H$_2$O microsphere	4 μm/200 nm	UV–Vis–NIR light	RhB	2.6	–	[97]
TiO$_2$ NS	130 nm/8 nm	–	MO	16.71	–	[195]
ZnO flower	1–2 μm/–	Hg lamp	RhB	125	–	[84]
ZnO hollowsphere	–/160 nm	Hg lamp	RhB	10.5	–	[196]
Fe$_2$O$_3$ hollowsphere	70 nm/–	UV light	MO	458	–	[101]
MoO$_{3-x}$ nanoplates	50–70 nm/> 20 nm	Sunlight	MB	1250	–	[74]
CuO NS	100–1000 nm/10–30 nm	UV light	MO	45.5	19.06 (NP)	[103]
CuO hollowsphere	500 nm/–	UV–Vis light	RhB	4.5	–	[99]
ZnS NS	–	Hg lamp	MO	500	–	[88]
ZnSe microsphere	1 μm/80 nm	Xe lamp	MO	40.41	16.66 (NP)	[91]
WS$_2$ NS	2–4 μm/100 nm	UV–Vis–NIR light	MO	7.5	–	[158]
CuS microsphere	2 μm/1–10 nm	Sunlight	MB	218.07	143.03 (NP)	[197]
ZrS$_2$ NS	10–30 nm/7 nm	Xe lamp	4-NP	31.68	–	[198]

DR degradation rate, *NS* nanosheet, *NP* nanoparticle, *NW* nanowhisker

However, the formation of 2D/0D (Fig. 8c, d) and 2D/1D (Fig. 8e, f) semiconducting heterostructures is much more popular. Representative examples are 2D Ti$_{0.91}$O$_2$ nanosheet/0D CdS quantum dot [151–153], 2D ZnO nanosheet/1D WO$_3$ nanorod [154], 2D ZnS nanosheet/0D ZnO nanograin [155], 2D ZnSe nanosheet/1D ZnO nanorod [156], 2D WS$_2$ nanosheet/0D WO$_3$ nanoparticles [157] and 2D WS$_2$ nanosheet/0D TiO$_2$ nanoparticles [158]. Heterojunctions formed with 0D up-converted materials (e.g., carbon dot) are also reported in 2D TiO$_2$ and WS$_2$ [159, 160]. These heterojunctions undoubtedly demonstrate efficient charge separation, larger available surface area and enhance visible light absorbability, hence improving their photocatalytic performances compared to the individual components and non-2D nanostructures

counterparts. Details of photocatalytic performances are found in Tables 1, 2, 3, 4, 5 and 6.

Apart from type II band alignment, the formation of *p–n* heterojunction is another effective approach to suppress the charge recombination [161]. In this approach, the contact between a *p*-type material with its *n*-type counterpart forms into a space charge layer and induces an internal electric field that can extend the probability of electron–hole separation (Fig. 10a). Meng et al. [162] fabricate a *p–n* heterojunction using *p*-2D MoS$_2$ and *n*-2D reduced graphene oxide (rGO) to improve the photocatalytic activity of MoS$_2$. Here, MoS$_2$ not only acts as a catalytic center but also a photocenter for absorbing solar light to generate charge carriers. The *p–n* junction activated the photocatalytic H$_2$ evolution performance of MoS$_2$

Table 5 Summary of pollutant degradation performances of 2D modified TMO&Cs

| Material	Dimension/thickness	Light source	Loading	Reaction solution	DR (% μmol $(gh)^{-1}$)	Comparison	Ref.
Elemental doping							
Mo-WO$_3$ NS	400–1600 nm/150 nm	Visible light	NA	RhB	12.5	–	[122]
B, F-codoped TiO$_2$NS	10 nm/2.5 nm	Xe lamp	NA	MB	18	–	[119]
C-ZnO flower	9 μm/~ 10 nm	Xe lamp	NA	RhB	1.5	–	[120]
ZnO NS/P-MoS$_2$ NS	–	Sunlight	NA	MB	222	–	[121]
Mn-CuO NS	–	Xe lamp	NA	MB	20.26	11.25 (CuO)	[123]
N-MoS$_2$ flower	–	Visible light	NA	RhB	134.2	–	[117]
Heterojunction with semiconductors							
WO$_3$ NS/Ag$_3$PO$_4$ NP	–	Xe lamp	–	MB	85.5	–	[168]
Ti0.$_{87}$O$_2$ NS/CdS pillar	100–500 μm/–	Xe lamp	–	MB	58	0.078 (N-TiO$_2$)	[151]
ZnO NS/WO$_3$ NR	–	Xe lamp	–	MB	533	–	[154]
MoS$_2$ NS/CdS NP	–	Xe lamp	2 mol % MoS$_2$	MB/RhB	40	–	[144]
MoS$_2$ flower/CdS NP	800 nm/–	Xe lamp	–	MB	97	–	[98]
MoS$_2$NS/CuS NP	–	Visible light	–	MB	104.21	–	[148]
Fe$_3$O$_4$@MoS$_2$ Core – Shell	–	Blue light	–	4-NP	285	–	[199]
MoS$_2$ NS/Ag$_3$PO$_4$ NP	–	Xe lamp	1 wt% MoS$_2$	RhB	93.9	–	[68]
MoS$_2$ NS/Ag$_3$PO$_4$ NP	–	Xe lamp	0.65 wt% MoS$_2$	RhB	18.78	–	[166]
MoS$_2$-r-GO NS/Ag$_3$PO$_4$ NP	–	Xe lamp	0.02 wt% MoS$_2$-r-GO	Phenol	1593.8	–	[167]
MoS$_2$ NS/TiO$_2$ NF	120–300 nm/–	UV light	–	MO	497.53	26.18 (MoS$_2$);	[143]
MoS$_2$ NS/TiO$_2$ NR	–	Xe lamp	50 wt% MoS$_2$	RhB	939.4	817.3 (MoS$_2$); 328.8 (TiO$_2$)	[56]
ZnS NS/ZnO NP	400–1000 nm/40 nm	W lamp	–	MB	6.4	4.6 (ZnS)	[155]
WS$_2$/WO$_3$ NP	–	Visible light	–	MB	378.9	–	[157]
Heterojunction with conductive materials							
TiO$_2$ NS/carbon QD	45–55 nm/6 nm	Visible light	–	RhB	19.83	8.3 (TiO$_2$ NP)	[159]
TiO$_2$ NS/g-C$_3$N$_4$ NS	38 nm/6 nm	UV–Vis light	–	MB	4.5	–	[149]
ZnO flower/Ag NP	–/10–19 nm	Hg lamp; Xe lamp	–	RhB	3.2	0.88 (ZnO NP)	[174]
ZnO NS/Ag NP	–	UV light	–	MO	389.5	–	[176]
Fe$_2$O$_3$ NS/r-GO NS	200 nm/–	Xe lamp	–	RhB	1.4	–	[98]
MoS$_2$ NS/g-C$_3$N$_4$ NS	–	–	0.05 wt% MoS$_2$	MO	40.7	–	[55]
MoSe$_2$ NS perpendicular to r-GO NS	–	Xe lamp	–	MB	70.34	15.4 (MoSe$_2$ NS/r-GO NS)	[181]
CoS NS/2D r-GO NS	~ 200–300 nm/~ 10–20 nm	Visible light	26.2 wt% CoS	MB	47.41	28.13 (CoS)	[182]

DR degradation rate, *NS* nanosheet, *NP* nanoparticle, *NR* nanorod, *NF* nanofiber, *QD* quantum dot

Table 6 Summary of antimicrobial disinfection performances of 2D TMO&Cs and their compounds

Material	Dimension/thickness	Light source	Target	Destruction rate	Ref.
Elemental doping					
B, F-codoped TiO_2 NS	10 nm/2.5 nm	Xe lamp	*E. coli*	99.5%	[119]
Heterojunction with semiconductors					
MoS_2 NS/ZnO flower	–	UV–Vis light	*E. coli*	45%	[138]
ZnO NS/NaYF4:Yb, Tm NC	–	Xe lamp	*E. coli, C. albicans, S. aureus*	MIC-50 µg mL^{-1}, 50 µg mL^{-1}, 100 µg mL^{-1}	[200]
Heterojunction with conductive materials					
TiO_2 NS/Ag NP	–	UV light	*Pseudomonas* sp. and *Bacillus* sp.	0.07% and 8×10^{-4} %	[201]

*NS* nanosheet, *NP* nanoparticle, *NC* nanocrystal, *MIC* minimal inhibitory concentration
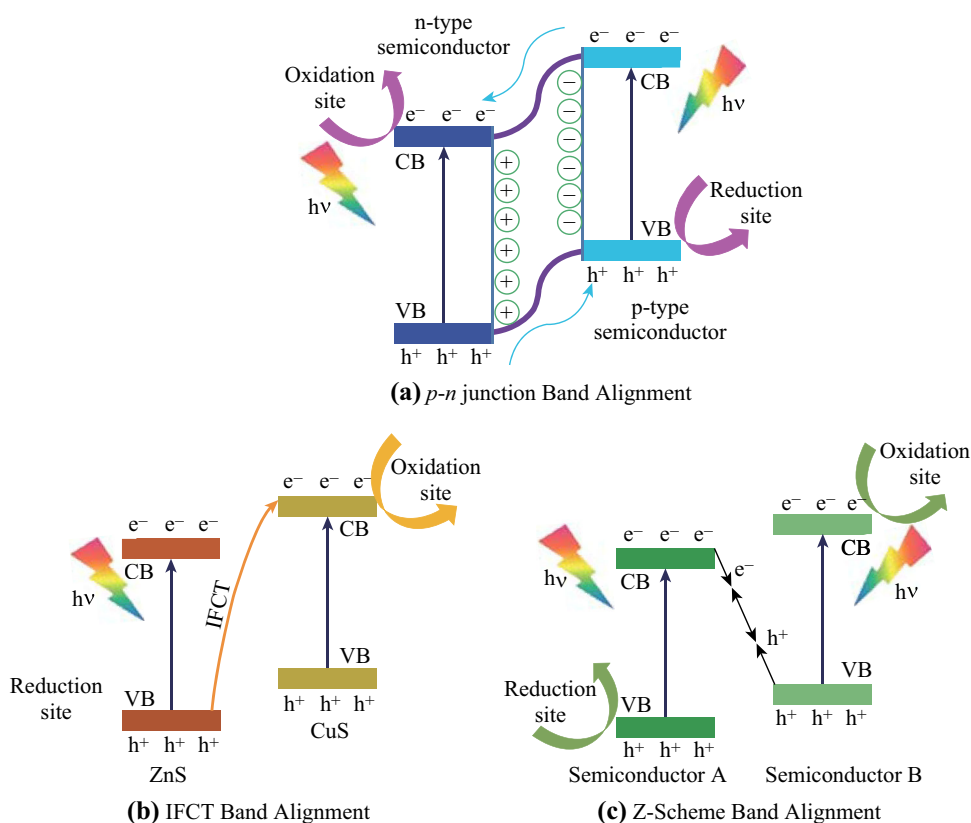
Fig. 10 Schematics of heterojunctions of **a** *p–n* junction, **b** IFCT and **c** Z-scheme. Reproduced with permission from Ref. [164, 166, 216]

although the production rate is still low (24.8 µmol (gh)$^{-1}$) [162]. Being inspired by this work, Xing et al. [163] fabricate a *p–n* heterojunction based on *n*-CdS and *p*-CdTe nanocrystals to enhance the visible light absorbability and charge recombination suppression. As a result, *n*-CdS became an efficient electron collector. 2D $Ti_{0.91}O_2$ nanosheet is then introduced to the *p–n* heterojunction acting as an electron sink and providing HER catalytic sites upon the formation of a type II band alignment heterojunction with *n*-CdS. The corresponding production rate is 463 µmol (gh)$^{-1}$, while no H_2 evolution occurs for bare titanate nanosheets [163].

There are some special charge transfer mechanisms when specific materials are coupled with 2D TMO&Cs. Zhang et al. [164] develop a visible light-driven photocatalyst based on a 2D ZnS nanosheet/0D CuS nanocluster heterojunction. Upon visible light irradiation, the photogenerated electrons in the VB of ZnS are transferred directly to the CB of CuS clusters due to the interfacial charge transfer (IFCT) mechanism (Fig. 10b). Such a mechanism has been commonly seen in the TMC-Cu(II) complex system upon the hybridization between the discrete energy levels of Cu(II) molecule and the continuous ones of TMC. Subsequently, the transferred electrons cause the partial reduction in CuS to Cu_2S and undergo effective reduction in H^+ to produce H_2 given that the potential of CuS/Cu_2S is well above that of H^+/H_2O [164]. Meanwhile, the holes in the VB of ZnS are consumed by the sacrificial agents. As the result, this IFCT phenomenon retards the recombination of photoexciton pairs due to space separation. The optimal CuS loading is determined to be about 2 mol % and the corresponding H_2 production rate is impressively ~ 4.2 mmol $(gh)^{-1}$, which is eight times larger than that of 2 mol % Cu-doped ZnS nanoparticles [164].

The heterojunction composed of 2D ZnO and CdS nanoparticles also exhibits special charge transfer process, namely Z-scheme (Fig. 10c). The recombination of the photogenerated electrons from the CB of ZnO and holes from the VB of CdS occurs at the interface, resulting in the retention of the photogenerated electrons in CdS with a higher CB position and holes in ZnO with a lower VB position. It is proposed that the metallic polar surface of ZnO may be a key factor in response to initiate the Z-scheme transfer process [165]. Similar observation is seen in the 2D MoS_2/0D Ag_3PO_4 heterojunction [166]. Conventionally, Ag_3PO_4 is an efficient photocatalyst but with weak chemical stability under prolonged light irradiation [68, 167]. When coupled with 2D MoS_2, efficient separation of photogenerated electron–hole pairs in Ag_3PO_4 is observed as 2D MoS_2 acts as an effective electron collector in the system. By comparing the band structures between MoS_2 and Ag_3PO_4, a heterojunction with the type II band alignment is expected to form, but the electron transfer direction is actually opposite, i.e., from MoS_2 to Ag_3PO_4. Zheng et al. propose that the charge transfer mechanism between MoS_2 and Ag_3PO_4 is predominated by the Z-scheme mechanism as the electrons from the CB of Ag_3PO_4 recombine with holes from the VB of MoS_2 using both the active species trapping and photoluminescence techniques [166]. With a small loading of MoS_2, the heterojunction demonstrates an almost double enhancement on the RhB and $\sim 50\%$ enhancement on phenol photodegradation performances compared to those of bare Ag_3PO_4 [68, 166, 167]. Such a Z-scheme mechanism may
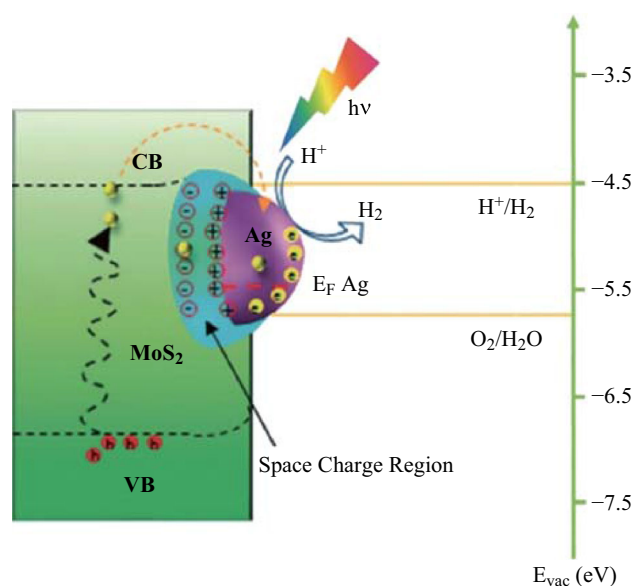
Fig. 11 Illustration of heterojunction between a 2D MoS_2 nanosheet and an Ag nanoparticle. Reproduced with permission of Ref. [175]

be also applied to other Ag_3PO_4-based heterojunctions such as the recently reported 2D WO_3/0D Ag_3PO_4 [168] and 2D $Ti_{0.91}O_2$/0D CdS heterojunctions [169].

3.3.2 Heterojunction with Conductive Materials

Similar to the heterojunctions formed with semiconductors, a rectified charge carrier transfer can occur in the Schottky barrier between a semiconductor and a metal, depending on their Fermi-level positions [170–172]. Upon light irradiation, electrons are generated in the CB of the semiconductor and lift its Fermi level to more negative values (Fig. 11) [173]. The resulted energetic difference at the semiconductor–metal interface drives the electrons from the CB of the semiconductor into the metal [173]. To incorporate into the heterojunctions with 2D TMO&Cs, the metals are either chemically co-synthesized with the semiconductor or synthesized individually first and then attached to the 2D TMO&C nanostructures for strong adhesion [174]. The metals are generally in the form of nanoparticle, and the weight ratios to the 2D TMO&Cs are optimized to avoid the surface overloading effect. In addition to the "electron sink" effect, some of the noble metal nanostructures exhibit localized surface plasmon resonance in the visible light spectrum, which can enhance the light harvesting efficiency of the heterojunction. In this case, the photogenerated electron–hole pairs are separated by the metal–semiconductor interface and the catalytic reactions hence take place on the surface of the plasmonic photocatalyst [175]. For instance, the incorporation of up to 1 wt% Ag nanoparticles into ZnO nanosheet results in an

additional visible light absorption peak in the region between 400 and 500 nm, which is ascribed to the localized surface plasmon resonance generated by Ag nanoparticles. A MO degradation rate of 389.5 μmol $(gh)^{-1}$ is demonstrated with ~ 50% enhancement compared to the ZnO nanoparticle counterpart [176]. Similar observations can be also seen 0.5 wt% Au–Pd/2D TiO_2 nanosheets, 20 wt% Ag/2D MoS_2 nanosheet as well as 1 wt% Cr/2D MoS_2 nanosheet [175, 177, 178]. It should be noted that some noble metals such as Pt are good catalyst by themselves [179]. Careful investigation should be carried out when revealing the mechanism for enhanced photocatalytic performances from the noble metal–semiconductor heterojunctions.

Conductive carbon-based low-dimensional nanomaterials are also excellent alternatives for metals to form heterojunctions with 2D TMO&Cs [180]. Due to their high conductivity and electron mobility as well as large surface area, these materials exhibit even better charge separation efficiencies compared to those of metals in many cases. So far 0D carbon dots, 1D carbon nanofibers and 2D graphene nanosheet have been investigated for possible candidates in 2D TMOs (e.g., TiO_2, $Ti_{0.91}O_2$ and Fe_2O_3) and TMCs (e.g., MoS_2, WS_2 $MoSe_2$ and CoS) [98, 137, 160, 169, 175, 181–184]. Detailed photocatalytic performances of these heterojunctions are summarized in Tables 1, 2, 3, 4, 5 and 6. As mentioned in the previous section, due to the nature of heterojunction interface, the heterojunctions of graphene with 2D TMO&Cs can possess a relatively stronger electronic and physical coupling effect, resulting in remarkable enhancement in the electron transfer process across the heterojunction and yielding superior photocatalytic activity [69]. Indeed, graphene itself is an excellent charge transfer medium which slows the recombination of photoexciton pairs, thus increasing charge transfer rate of electrons and surface adsorbed amount of chemical molecules through the π–π interaction [185, 186]. Heterojunctioning graphene in 2D TMO&Cs is generally realized by hydrothermal/solvothermal and microwave irradiation synthesis approaches [136, 187]. During the synthesis, graphene oxide and transition metal salts are the initial materials, and then, both of them are reduced to graphene nanosheet and 2D TMO&Cs, respectively. Compared to 0D metal nanoparticle-based heterojunctions, the lateral dimension of graphene nanosheets is much larger than those of 2D TMO&Cs, leading to a large interfacial contact and hence improved electron transfer across heterojunction. In addition, the loading of graphene can be as large as 30–40 wt%, ensuring much better photogenerated charge separation efficiency [98, 181, 182, 185–187].

Recently, the utilization of metallic 2D TMCs in the heterojunction has attracted great interest. 2D MX_2 (e.g.,

MoS_2 and WS_2) with metallic 1T crystal structures is typical representatives [55, 188]. As mentioned in the previous section, 1T 2D MX_2 has a very high conductivity which exhibits improved charge transfer kinetics. More importantly, it provides additional active sites for H_2 production on its basal plane, making it an efficient HER catalyst. When coupling with semiconductor as a co-catalyst, the electrons generated on the semiconductor can directly migrate to the basal sites for catalytic reactions, unlike the case for 2H MX_2. This greatly shortens the diffuse length of electrons and hence reduces the chance of charge recombination [188]. Taking 1T MoS_2, for example, the hydrogen production rate of 1T MoS_2/TiO_2 reaches 2 mmol $(gh)^{-1}$, which is 5 and 8 times higher than those of bare TiO_2 (400 μmol $(gh)^{-1}$) and 2H MoS_2/TiO_2 (250 μmol $(gh)^{-1}$), respectively [188].

3.3.3 Synthesis Techniques of 2D TMO&C-Based Heterojunction Photocatalysts

Physical mixture through grounding is the most straightforward approach to realize 2D TMO&C-based heterojunctions. However, the poor interfacial contact between materials is the major concern. Other physical approaches such as magnetic stirring and ultrasonication can improve the quality of the contacts [189–191]. Binding chemicals such as poly(ethyleneimine) (PEI) are also used for inducing higher degrees of adhesion in the heterojunctions during the hydrothermal/solvothermal and chemical bath synthesis [98, 162, 164, 176, 177, 181, 188]. Interestingly, there are special synthesis approaches for particular heterojunctions. Examples include ion exchange method for 2D ZnS/Ag_2S by replacing Zn^{2+} with Ag^+ [192], layer-by-layer self-assembly technique for 2D $Ti_{0.91}O_2/CdS$ using poly(methyl methacrylate) (PMMA) spheres as the template [169, 187] and calcination of TMCs in an oxygen-rich environment for creating 2D WS_2/WO_3 and MoS_2/MoO_3 contacts [112, 155]. Microwave irradiation synthesis is reported to be highly effective in forming heterojunctions with graphene and carbon dots [160, 187], while high-power UV irradiation can transform adsorbed noble metal ions into nanoparticles on the surface of 2D TMOs during the semiconductor–metal heterojunction formation [174].

4 Summary and Outlooks

The application of both layered and non-layered 2D TMO&Cs in photocatalysts has received rapid momentum in recent years. The properties of 2D TMO&Cs have shown distinct advantages for photocatalytic HER, pollutant degradation, carbon reduction and microbial

disinfection process. Through a significant number of demonstrations, the larger surface area of 2D nanostructures and their 3D derivative hierarchical structures offer more reaction sites for photocatalytic reactions and facilitate the charge migration for improving photocatalytic reaction kinetics. The unique tunable band structures in 2D TMO&Cs lead to more thermodynamically favorable redox reactions during the photocatalytic processes. Furthermore, the predominant exposed crystal facets provided by the 2D geometrical configuration also greatly improve the photocatalytic performance.

The investigation of 2D TMO&C-based photocatalysts is still in its early stage compared with the relatively mature 1D and nanoparticle-based photocatalytic systems. Many opportunities are just emerging, and significant advances are expected in the near future. The key for accelerating the research field is to produce 2D TMO&Cs especially with the non-layered crystal systems in a facile and high-yield manner. The further optimization of deposition parameters for vapor-phase synthesis, such as the amount of source material and vaporization energy/temperature, is needed to conduct for maximizing the production yield that is suitable for efficient photocatalytic reactions. Through possible implementation of novel templates and grow directing agents, liquid-phase synthesis techniques can also offer great opportunities for large scale production of 2D TMO&Cs with strong morphological controllability, which will be of great importance for developing efficient 2D TMO&C-based photocatalysts met with the industry standard.

The improvement strategies of photocatalytic performances are also critically discussed in this paper, particularly focusing on the approaches of elemental doping, surface functionalization and heterojunctions with both semiconducting and conductive materials. Compared to other 2D/low-dimensional heterojunctions, the 2D/2D system is suggested to exhibit greater stability and better coupling heterointerfaces, which facilitates the photoinduced charge transfer and separation. However, the related synergetic effects are currently less studied and should be further explored for designing new 2D/2D heterojunctions with extraordinary photocatalytic properties. In addition, the tuning of stoichiometry in 2D TMO&Cs can greatly influence their electronic band structures, resulting in narrowing bandgap energies and possibly producing surface plasmon resonance in the visible light region when their free charge carrier concentrations are large enough. The implementation of the sub-stoichiometric phase of 2D TMO&Cs in photocatalytic applications can possibly offer various benefits including the improvement of the light harvesting and photoexcited charge carrier transfer.

All in all, possibilities of new insights in 2D TMO&C-based photocatalysts are plenty and require significant resources and attention to discover new phenomena that harness the unique strength provided by 2D materials.

References

1. Z. Zou, J. Ye, K. Sayama, H. Arakawa, Direct splitting of water under visible light irradiation with an oxide semiconductor photocatalyst. Nature **414**(6864), 625–627 (2001). https://doi.org/10.1038/414625a
2. D. Bahnemann, Photocatalytic water treatment: solar energy applications. Sol. Energy **77**(5), 445–459 (2004). https://doi.org/10.1016/j.solener.2004.03.031
3. K. Maeda, K. Teramura, D. Lu, T. Takata, N. Saito, Y. Inoue, K. Domen, Photocatalyst releasing hydrogen from water. Nature **440**(7082), 295 (2006). https://doi.org/10.1038/440295a
4. T.P. Yoon, M.A. Ischay, J. Du, Visible light photocatalysis as a greener approach to photochemical synthesis. Nat. Chem. **2**(7), 527–532 (2010). https://doi.org/10.1038/nchem.687
5. W. Li, L. Li, H. Xiao, R. Qi, Y. Huang, Z. Xie, X. Jing, H. Zhang, Iodo-BODIPY: a visible-light-driven, highly efficient and photostable metal-free organic photocatalyst. RSC Adv. **3**(32), 13417–13421 (2013). https://doi.org/10.1039/c3ra40932e
6. H. Zhang, G. Chen, D.W. Bahnemann, Photoelectrocatalytic materials for environmental applications. J. Mater. Chem. **19**(29), 5089–5121 (2009). https://doi.org/10.1039/b821991e
7. K. Maeda, K. Domen, Photocatalytic water splitting: recent progress and future challenges. J. Phys. Chem. Lett. **1**(18), 2655–2661 (2010). https://doi.org/10.1021/jz1007966
8. M.D. Hernández-Alonso, F. Fresno, S. Suárez, J.M. Coronado, Development of alternative photocatalysts to TiO_2: challenges and opportunities. Energy Environ. Sci. **2**(12), 1231–1257 (2009). https://doi.org/10.1039/b907933e
9. Y. Izumi, Recent advances in the photocatalytic conversion of carbon dioxide to fuels with water and/or hydrogen using solar energy and beyond. Coordin. Chem. Rev. **257**(1), 171–186 (2013). https://doi.org/10.1016/j.ccr.2012.04.018
10. C.S. Turchi, D.F. Ollis, Photocatalytic degradation of organic water contaminants: mechanisms involving hydroxyl radical attack. J. Catal. **122**(1), 178–192 (1990). https://doi.org/10.1016/0021-9517(90)90269-P
11. M. Pelaez, N.T. Nolan, S.C. Pillai, M.K. Seery, P. Falaras et al., A review on the visible light active titanium dioxide photocatalysts for environmental applications. Appl. Catal. B **125**(33), 331–349 (2012). https://doi.org/10.1016/j.apcatb.2012.05.036
12. U. Akpan, B. Hameed, Parameters affecting the photocatalytic degradation of dyes using TiO_2-based photocatalysts: a review. J. Hazard. Mater. **170**(2), 520–529 (2009). https://doi.org/10.1016/j.jhazmat.2009.05.039
13. X. Meng, Z. Zhang, X. Li, Synergetic photoelectrocatalytic reactors for environmental remediation: a review. J. Photochem. Photobiol. C **24**, 83–101 (2015). https://doi.org/10.1016/j.jphotochemrev.2015.07.003

14. H. Tong, S. Ouyang, Y. Bi, N. Umezawa, M. Oshikiri, J. Ye, Nano-photocatalytic materials: possibilities and challenges. Adv. Mater. **24**(2), 229–251 (2012). https://doi.org/10.1002/adma.201102752

15. S. Banerjee, S.K. Mohapatra, P.P. Das, M. Misra, Synthesis of coupled semiconductor by filling 1D TiO$_2$ nanotubes with CdS. Chem. Mater. **20**(21), 6784–6791 (2008). https://doi.org/10.1021/cm802282t

16. Y. Wu, H. Yan, P. Yang, Semiconductor nanowire array: potential substrates for photocatalysis and photovoltaics. Top. Catal. **19**(2), 197–202 (2002). https://doi.org/10.1023/A:1015260008046

17. A. Fujishima, T.N. Rao, D.A. Tryk, Titanium dioxide photocatalysis. J. Photochem. Photobiol. C **1**(1), 1–21 (2000). https://doi.org/10.1016/S1389-5567(00)00002-2

18. A. Fujishima, X. Zhang, D.A. Tryk, TiO$_2$ photocatalysis and related surface phenomena. Surf. Sci. Rep. **63**(12), 515–582 (2008). https://doi.org/10.1016/j.surfrep.2008.10.001

19. J. Yu, X. Yu, Hydrothermal synthesis and photocatalytic activity of zinc oxide hollow spheres. Environ. Sci. Technol. **42**(13), 4902–4907 (2008). https://doi.org/10.1021/es800036n

20. Y. Chen, C. Lu, L. Xu, Y. Ma, W. Hou, J.-J. Zhu, Single-crystalline orthorhombic molybdenum oxide nanobelts: synthesis and photocatalytic properties. CrystEngComm **12**(11), 3740–3747 (2010). https://doi.org/10.1039/c000744g

21. J.Z. Ou, R.A. Rani, S. Balendhran, A.S. Zoolfakar, M.R. Field, S. Zhuiykov, A.P. O'Mullane, K. Kalantar-zadeh, Anodic formation of a thick three-dimensional nanoporous WO$_3$ film and its photocatalytic property. Electrochem. Commun. **27**(1), 128–132 (2013). https://doi.org/10.1016/j.elecom.2012.11.009

22. H. Jiang, M. Nagai, K. Kobayashi, Enhanced photocatalytic activity for degradation of methylene blue over V$_2$O$_5$/BiVO$_4$ composite. J. Alloys Compd. **479**(1), 821–827 (2009). https://doi.org/10.1016/j.jallcom.2009.01.051

23. S. Xu, D.D. Sun, Significant improvement of photocatalytic hydrogen generation rate over TiO$_2$ with deposited CuO. Int. J. Hydrog. Energy **34**(15), 6096–6104 (2009). https://doi.org/10.1016/j.ijhydene.2009.05.119

24. J. Bandara, C. Udawatta, C. Rajapakse, Highly stable CuO incorporated TiO$_2$ catalyst for photocatalytic hydrogen production from H$_2$O. Photoch. Photobiol. Sci. **4**(11), 857–861 (2005). https://doi.org/10.1039/b507816d

25. S.J. Moniz, S.A. Shevlin, D.J. Martin, Z.-X. Guo, J. Tang, Visible-light driven heterojunction photocatalysts for water splitting—a critical review. Energy Environ. Sci. **8**(3), 731–759 (2015). https://doi.org/10.1039/C4EE03271C

26. J.S. Hu, L.L. Ren, Y.G. Guo, H.P. Liang, A.M. Cao, L.J. Wan, C.L. Bai, Mass production and high photocatalytic activity of ZnS nanoporous nanoparticles. Angew. Chem. Int. Ed. **117**(8), 1295–1299 (2005). https://doi.org/10.1002/ange.200462057

27. J.F. Reber, K. Meier, Photochemical production of hydrogen with zinc sulfide suspensions. J. Phys. Chem. **88**(24), 5903–5913 (1984). https://doi.org/10.1021/j150668a032

28. M. Kanemoto, T. Shiragami, C. Pac, S. Yanagida, Semiconductor photocatalysis. Effective photoreduction of carbon dioxide catalyzed by ZnS quantum crystallites with low density of surface defects. J. Phys. Chem. **96**(8), 3521–3526 (1992). https://doi.org/10.1021/j100187a062

29. M. Sathish, B. Viswanathan, R. Viswanath, Alternate synthetic strategy for the preparation of CdS nanoparticles and its exploitation for water splitting. Int. J. Hydrog. Energy **31**(7), 891–898 (2006). https://doi.org/10.1016/j.ijhydene.2005.08.002

30. H. Yin, Y. Wada, T. Kitamura, S. Yanagida, Photoreductive dehalogenation of halogenated benzene derivatives using ZnS or CdS nanocrystallites as photocatalysts. Environ. Sci. Technol. **35**(1), 227–231 (2001). https://doi.org/10.1021/es001114d

31. J.F. Callejas, J.M. McEnaney, C.G. Read, J.C. Crompton, A.J. Biacchi, E.J. Popczun, T.R. Gordon, N.S. Lewis, R.E. Schaak, Electrocatalytic and photocatalytic hydrogen production from acidic and neutral-pH aqueous solutions using iron phosphide nanoparticles. ACS Nano **8**(11), 11101–11107 (2014). https://doi.org/10.1021/nn5048553

32. J.S. Jang, D.J. Ham, N. Lakshminarasimhan, W.Y. Choi, J.S. Lee, Role of platinum-like tungsten carbide as cocatalyst of CdS photocatalyst for hydrogen production under visible light irradiation. Appl. Catal. A **346**(1), 149–154 (2008). https://doi.org/10.1016/j.apcata.2008.05.020

33. Y.K. Kim, H. Park, Light-harvesting multi-walled carbon nanotubes and CdS hybrids: application to photocatalytic hydrogen production from water. Energy Environ. Sci. **4**(3), 685–694 (2011). https://doi.org/10.1039/C0EE00330A

34. C. Han, M.-Q. Yang, N. Zhang, Y.-J. Xu, Enhancing the visible light photocatalytic performance of ternary CdS-(graphene-Pd) nanocomposites via a facile interfacial mediator and co-catalyst strategy. J. Mater. Chem. A **2**(45), 19156–19166 (2014). https://doi.org/10.1039/C4TA04151H

35. K. Kalantar-zadeh, J.Z. Ou, T. Daeneke, M.S. Strano, M. Pumera, S.L. Gras, Two-dimensional transition metal dichalcogenides in biosystems. Adv. Funct. Mater. **25**(32), 5086–5099 (2015). https://doi.org/10.1002/adfm.201500891

36. K. Kalantar-zadeh, J.Z. Ou, T. Daeneke, A. Mitchell, T. Sasaki, M.S. Fuhrer, Two dimensional and layered transition metal oxides. Appl. Mater. Today **5**, 73–89 (2016). https://doi.org/10.1016/j.apmt.2016.09.012

37. Q.H. Wang, K. Kalantar-Zadeh, A. Kis, J.N. Coleman, M.S. Strano, Electronics and optoelectronics of two-dimensional transition metal dichalcogenides. Nat. Nanotechnol. **7**(11), 699–712 (2012). https://doi.org/10.1038/nnano.2012.193

38. B. Luo, G. Liu, L. Wang, Recent advances in 2D materials for photocatalysis. Nanoscale **8**(13), 6904–6920 (2016). https://doi.org/10.1039/C6NR00546B

39. Y. Sun, Z. Sun, S. Gao, H. Cheng, Q. Liu, F. Lei, S. Wei, Y. Xie, All-surface-atomic-metal chalcogenide sheets for high-efficiency visible-light photoelectrochemical water splitting. Adv. Energy Mater. **4**(1), 130611 (2014). https://doi.org/10.1002/aenm.201300611

40. M. Nasilowski, B. Mahler, E. Lhuillier, S. Ithurria, B. Dubertret, Two-dimensional colloidal nanocrystals. Chem. Rev. **116**(18), 10934–10982 (2016). https://doi.org/10.1021/acs.chemrev.6b00164

41. W.-J. Ong, L.-L. Tan, S.-P. Chai, S.-T. Yong, A.R. Mohamed, Highly reactive 001 facets of TiO$_2$-based composites: synthesis, formation mechanism and characterization. Nanoscale **6**(4), 1946–2008 (2014). https://doi.org/10.1039/c3nr04655a

42. H. Xu, S. Ouyang, P. Li, T. Kako, J. Ye, High-active anatase TiO$_2$ nanosheets exposed with 95% 100 facets toward efficient H$_2$ evolution and CO$_2$ photoreduction. ACS Appl. Mater. Interfaces **5**(4), 1348–1354 (2013). https://doi.org/10.1021/am302631b

43. J. Yu, J. Low, W. Xiao, P. Zhou, M. Jaroniec, Enhanced photocatalytic CO$_2$-reduction activity of anatase TiO$_2$ by coexposed 001 and 101 facets. J. Am. Chem. Soc. **136**(25), 8839–8842 (2014). https://doi.org/10.1021/ja5044787

44. A. Splendiani, L. Sun, Y. Zhang, T. Li, J. Kim, C.Y. Chim, G. Galli, F. Wang, Emerging photoluminescence in monolayer MoS$_2$. Nano Lett. **10**(4), 1271–1275 (2010). https://doi.org/10.1021/nl903868w

45. H.R. Gutierrez, N. Perea-López, A. Elías, A. Berkdemir, B. Wang, et al., Extraordinary room-temperature photoluminescence in triangular WS$_2$ monolayers. Nano Lett. **13**(8), 3447–3454 (2013). http://pubs.acs.org/doi/abs/10.1021/nl3026357

46. H. Lin, C. Wang, J. Wu, Z. Xu, Y. Huang, C. Zhang, Colloidal synthesis of MoS_2 quantum dots: size-dependent tunable photoluminescence and bioimaging. New J. Chem. 39(11), 8492–8497 (2015). https://doi.org/10.1039/C5NJ01698C

47. Y. Wang, J.Z. Ou, S. Balendhran, A.F. Chrimes, M. Mortazavi et al., Electrochemical control of photoluminescence in two-dimensional MoS_2 nanoflakes. ACS Nano 7(11), 10083–10093 (2013). https://doi.org/10.1021/nn4041987

48. Y. Peng, L. Shang, T. Bian, Y. Zhao, C. Zhou, H. Yu, L.Z. Wu, C.H. Tung, T. Zhang, Flower-like CdSe ultrathin nanosheet assemblies for enhanced visible-light-driven photocatalytic H_2 production. Chem. Commun. 51(22), 4677–4680 (2015). https://doi.org/10.1039/C5CC00136F

49. X. Chen, Y. Zhou, Q. Liu, Z. Li, J. Liu, Z. Zou, Ultrathin, single-crystal WO_3 nanosheets by two-dimensional oriented attachment toward enhanced photocatalystic reduction of CO_2 into hydrocarbon fuels under visible light. ACS Appl. Mater. Interfaces 4(7), 3372–3377 (2012). https://doi.org/10.1021/am300661s

50. J.A. Scher, J.M. Elward, A. Chakraborty, Shape matters: effect of 1D, 2D, and 3D isovolumetric quantum confinement in semiconductor nanoparticles. J. Phys. Chem. C 120(43), 24999–25009 (2016). https://doi.org/10.1021/acs.jpcc.6b06728

51. I. Robel, M. Kuno, P.V. Kamat, Size-dependent electron injection from excited CdSe quantum dots into TiO_2 nanoparticles. J. Am. Chem. Soc. 129(14), 4136–4137 (2007). https://doi.org/10.1021/ja070099a

52. Y. Wang, J.Z. Ou, A.F. Chrimes, B.J. Carey, T. Daeneke et al., Plasmon resonances of highly doped two-dimensional MoS_2. Nano Lett. 15(2), 883–890 (2015). https://doi.org/10.1021/nl503563g

53. M.M. Alsaif, K. Latham, M.R. Field, D.D. Yao, N.V. Medehkar et al., Tunable plasmon resonances in two-dimensional molybdenum oxide nanoflakes. Adv. Mater. 26(23), 3931–3937 (2014). https://doi.org/10.1002/adma.201306097

54. C. Tan, H. Zhang, Wet-chemical synthesis and applications of non-layer structured two-dimensional nanomaterials. Nat. Commun. 6, 7873 (2015). https://doi.org/10.1038/ncomms8873

55. B. Mahler, V. Hoepfner, K. Liao, G.A. Ozin, Colloidal synthesis of 1T-WS_2 and 2H-WS_2 nanosheets: applications for photocatalytic hydrogen evolution. J. Am. Chem. Soc. 136(40), 14121–14127 (2014). https://doi.org/10.1021/ja506261t

56. W. Zhou, Z. Yin, Y. Du, X. Huang, Z. Zeng, Z. Fan, H. Liu, J. Wang, H. Zhang, Synthesis of few-layer MoS_2 nanosheet-coated TiO_2 nanobelt heterostructures for enhanced photocatalytic activities. Small 9(1), 140–147 (2013). https://doi.org/10.1002/smll.201201161

57. Q. Li, N. Zhang, Y. Yang, G. Wang, D.H. Ng, High efficiency photocatalysis for pollutant degradation with MoS_2/C_3N_4 heterostructures. Langmuir 30(29), 8965–8972 (2014). https://doi.org/10.1021/la502033t

58. R. Kappera, D. Voiry, S.E. Yalcin, B. Branch, G. Gupta, A.D. Mohite, M. Chhowalla, Phase-engineered low-resistance contacts for ultrathin MoS_2 transistors. Nat. Mater. 13(12), 1128–1134 (2014). https://doi.org/10.1038/nmat4080

59. M. Acerce, D. Voiry, M. Chhowalla, Metallic 1T phase MoS_2 nanosheets as supercapacitor electrode materials. Nat. Nanotechnol. 10(4), 313–318 (2015). https://doi.org/10.1038/nnano.2015.40

60. M.A. Lukowski, A.S. Daniel, F. Meng, A. Forticaux, L. Li, S. Jin, Enhanced hydrogen evolution catalysis from chemically exfoliated metallic MoS_2 nanosheets. J. Am. Chem. Soc. 135(28), 10274–10277 (2013). https://doi.org/10.1021/ja404523s

61. Y.-C. Lin, D.O. Dumcenco, Y.-S. Huang, K. Suenaga, Atomic mechanism of the semiconducting-to-metallic phase transition in single-layered MoS_2. Nat. Nanotechnol. 9(5), 391–396 (2014). https://doi.org/10.1038/nnano.2014.64

62. J. Xie, J. Zhang, S. Li, F. Grote, X. Zhang et al., Controllable disorder engineering in oxygen-incorporated MoS_2 ultrathin nanosheets for efficient hydrogen evolution. J. Am. Chem. Soc. 135(47), 17881–17888 (2013). https://doi.org/10.1021/ja408329q

63. D. Kozawa, R. Kumar, A. Carvalho, A.K. Kumar, W. Zhao et al., Photocarrier relaxation in two-dimensional semiconductors. Nat. Commun. 5, 4543 (2014). https://doi.org/10.1038/ncomms5543

64. H. Shi, R. Yan, S. Bertolazzi, J. Brivio, B. Gao, A. Kis, D. Jena, H.G. Xing, L. Huang, Exciton dynamics in suspended monolayer and few-layer MoS_2 2D crystals. ACS Nano 7(2), 1072–1080 (2013). https://doi.org/10.1021/nn303973r

65. P.D. Cunningham, K.M. McCreary, A.T. Hanbicki, M. Currie, B.T. Jonker, L.M. Hayden, Charge trapping and exciton dynamics in large-area CVD grown MoS_2. J. Phys. Chem. C 120(10), 5819–5826 (2016). https://doi.org/10.1021/acs.jpcc.6b00647

66. H. Liu, J. Lu, Exciton dynamics in tungsten dichalcogenide monolayers. Phys. Chem. Chem. Phys. 19(27), 17877–17882 (2017). https://doi.org/10.1039/C7CP02510F

67. C. Pöllmann, P. Steinleitner, U. Leierseder, P. Nagler, G. Plechinger et al., Resonant internal quantum transitions and femtosecond radiative decay of excitons in monolayer WSe_2. Nat. Mater. 14(9), 889–893 (2015). https://doi.org/10.1038/nmat4356

68. Y. Song, Y. Lei, H. Xu, C. Wang, J. Yan et al., Synthesis of few-layer MoS_2 nanosheet-loaded Ag_3PO_4 for enhanced photocatalytic activity. Dalton Trans. 44(7), 3057–3066 (2015). https://doi.org/10.1039/C4DT03242J

69. Q. Xiang, J. Yu, M. Jaroniec, Synergetic effect of MoS_2 and graphene as cocatalysts for enhanced photocatalytic H_2 production activity of TiO_2 nanoparticles. J. Am. Chem. Soc. 134(15), 6575–6578 (2012). https://doi.org/10.1021/ja302846n

70. M. Shen, Z. Yan, L. Yang, P. Du, J. Zhang, B. Xiang, MoS_2 nanosheet/TiO_2 nanowire hybrid nanostructures for enhanced visible-light photocatalytic activities. Chem. Commun. 50(97), 15447–15449 (2014). https://doi.org/10.1039/C4CC07351G

71. X. Duan, C. Wang, A. Pan, R. Yu, X. Duan, Two-dimensional transition metal dichalcogenides as atomically thin semiconductors: opportunities and challenges. Chem. Soc. Rev. 44(24), 8859–8876 (2015). https://doi.org/10.1039/C5CS00507H

72. S. Balendhran, S. Walia, H. Nili, J.Z. Ou, S. Zhuiykov, R.B. Kaner, S. Sriram, M. Bhaskaran, K. Kalantar-zadeh, Two-dimensional molybdenum trioxide and dichalcogenides. Adv. Funct. Mater. 23(32), 3952–3970 (2013). https://doi.org/10.1002/adfm.201300125

73. D.D. Yao, J.Z. Ou, K. Latham, S. Zhuiykov, A.P. O'Mullane, K. Kalantar-zadeh, Electrodeposited α-and β-phase MoO_3 films and investigation of their gasochromic properties. Cryst. Growth Des. 12(4), 1865–1870 (2012). https://doi.org/10.1021/cg201500b

74. V.V. Kumar, K. Gayathri, S.P. Anthony, Synthesis of α-MoO_3 nanoplates using organic aliphatic acids and investigation of sunlight enhanced photodegradation of organic dyes. Mater. Res. Bull. 76(4706), 147–154 (2016). https://doi.org/10.1016/j.materresbull.2015.12.016

75. C. Bhandari, W.R. Lambrecht, M. van Schilfgaarde, Quasiparticle self-consistent GW calculations of the electronic band structure of bulk and monolayer V_2O_5. Phys. Rev. B 91(12), 125116 (2015). https://doi.org/10.1103/PhysRevB.91.125116

76. T. Puangpetch, S. Chavadej, T. Sreethawong, Mesoporous-assembled V_2O_5 nanosheet synthesized via a surfactant-modified sol–gel technique and its photocatalytic H_2 production

activity under visible light irradiation. Powder Technol. **208**(1), 37–41 (2011). https://doi.org/10.1016/j.powtec.2010.11.039

77. L. Wang, T. Sasaki, Titanium oxide nanosheets: graphene analogues with versatile functionalities. Chem. Rev. **114**(19), 9455–9486 (2014). https://doi.org/10.1021/cr400627u

78. T. Zhu, S.-P. Gao, The stability, electronic structure, and optical property of TiO_2 polymorphs. J. Phys. Chem. C **118**(21), 11385–11396 (2014). https://doi.org/10.1021/jp412462m

79. D.O. Scanlon, C.W. Dunnill, J. Buckeridge, S.A. Shevlin, A.J. Logsdail et al., Band alignment of rutile and anatase TiO_2. Nat. Mater. **12**(9), 798–801 (2013). https://doi.org/10.1038/nmat3697

80. Z.R. Tian, J.A. Voigt, J. Liu, B. Mckenzie, M.J. Mcdermott, M.A. Rodriguez, H. Konishi, H. Xu, Complex and oriented ZnO nanostructures. Nat. Mater. **2**(12), 821–826 (2003). https://doi.org/10.1038/nmat1014

81. Z.L. Wang, Nanostructures of zinc oxide. Mater. Today **7**(6), 26–33 (2004). https://doi.org/10.1016/S1369-7021(04)00286-X

82. M. Kalay, H. Kart, S.Ö. Kart, T. Çağın, Elastic properties and pressure induced transitions of ZnO polymorphs from first-principle calculations. J. Alloys Compd. **484**(1), 431–438 (2009). https://doi.org/10.1016/j.jallcom.2009.04.116

83. C. Tusche, H. Meyerheim, J. Kirschner, Observation of depolarized ZnO (0001) monolayers: formation of unreconstructed planar sheets. Phys. Rev. Lett. **99**(2), 026102 (2007). https://doi.org/10.1103/PhysRevLett.99.026102

84. Y. Miao, H. Zhang, S. Yuan, Z. Jiao, X. Zhu, Preparation of flower-like ZnO architectures assembled with nanosheets for enhanced photocatalytic activity. J. Colloid Interface Sci. **462**, 9–18 (2016). https://doi.org/10.1016/j.jcis.2015.09.064

85. X. Zhao, F. Lou, M. Li, X. Lou, Z. Li, J. Zhou, Sol–gel-based hydrothermal method for the synthesis of 3D flower-like ZnO microstructures composed of nanosheets for photocatalytic applications. Ceram. Int. **40**(4), 5507–5514 (2014). https://doi.org/10.1016/j.ceramint.2013.10.140

86. H. Wu, Q. Xie, L. An, P. Jin, D.-L. Peng, C. Huang, H. Wan, Facile preparation of porous flower-like ZnO microspheres with excellent photocatalytic performance. Mater. Lett. **139**, 393–396 (2015). https://doi.org/10.1016/j.matlet.2014.10.101

87. N. Bao, L. Shen, T. Takata, K. Domen, Self-templated synthesis of nanoporous CdS nanostructures for highly efficient photocatalytic hydrogen production under visible light. Chem. Mater. **20**(1), 110–117 (2007). https://doi.org/10.1021/cm7029344

88. Q. Wu, F. Sun, Photochemical synthesis of ZnS nanosheet and its use in photodegradation of organic pollutants, in *2010 4th International Conference on Bioinformatics and Biomedical Engineering (iCBBE)* (2010), pp. 1–4. https://doi.org/10.1109/ICBBE.2010.5517517

89. Y.-N. Xu, W. Ching, Electronic, optical, and structural properties of some wurtzite crystals. Phys. Rev. B **48**(7), 4335 (1993). https://doi.org/10.1103/PhysRevB.48.4335

90. B. Feng, J. Yang, J. Cao, L. Yang, M. Gao, M. Wei, H. Zhai, Y. Sun, H. Song, Growth mechanism, optical and photocatalytic properties of the ZnSe nanosheets constructed by the nanoparticles. J. Alloys Compd. **555**(555), 241–245 (2013). https://doi.org/10.1016/j.jallcom.2012.12.074

91. X. Wu, R. Xu, R. Zhu, R. Wu, B. Zhang, Converting 2D inorganic-organic ZnSe-DETA hybrid nanosheets into 3D hierarchical nanosheet-based ZnSe microspheres with enhanced visible-light-driven photocatalytic performances. Nanoscale **7**(21), 9752–9759 (2015). https://doi.org/10.1039/C5NR02329G

92. Y. Xu, W. Zhao, R. Xu, Y. Shi, B. Zhang, Synthesis of ultrathin CdS nanosheets as efficient visible-light-driven water splitting photocatalysts for hydrogen evolution. Chem. Commun. **49**(84), 9803–9805 (2013). https://doi.org/10.1039/c3cc46342g

93. Q. Xiang, B. Cheng, J. Yu, Hierarchical porous CdS nanosheet-assembled flowers with enhanced visible-light photocatalytic

94. H. Zheng, J.Z. Ou, M.S. Strano, R.B. Kaner, A. Mitchell, K. Kalantar-zadeh, Nanostructured tungsten oxide-properties, synthesis, and applications. Adv. Funct. Mater. **21**(12), 2175–2196 (2011). https://doi.org/10.1002/adfm.201002477

95. D. Sanchez-Martinez, C. Gomez-Solis, L.M. Torres-Martinez, CTAB-assisted ultrasonic synthesis, characterization and photocatalytic properties of WO_3. Mater. Res. Bull. **61**, 165–172 (2015). https://doi.org/10.1016/j.materresbull.2014.10.034

96. J. Huang, L. Xiao, X. Yang, WO_3 nanoplates, hierarchical flower-like assemblies and their photocatalytic properties. Mater. Res. Bull. **48**(8), 2782–2785 (2013). https://doi.org/10.1016/j.materresbull.2013.04.022

97. X.-N. Song, C.-Y. Wang, W.-K. Wang, X. Zhang, N.-N. Hou, H.-Q. Yu, A dissolution-regeneration route to synthesize blue tungsten oxide flowers and their applications in photocatalysis and gas sensing. Adv. Mater. Interfaces **3**(1), 1500417 (2016). https://doi.org/10.1002/admi.201500417

98. S. Han, L. Hu, Z. Liang, S. Wageh, A.A. Al-Ghamdi, Y. Chen, X. Fang, One-step hydrothermal synthesis of 2D hexagonal nanoplates of α-Fe_2O_3/graphene composites with enhanced photocatalytic activity. Adv. Funct. Mater. **24**(36), 5719–5727 (2014). https://doi.org/10.1002/adfm.201401279

99. J. Zhu, X. Qian, From 2-D CuO nanosheets to 3-D hollow nanospheres: interface-assisted synthesis, surface photovoltage properties and photocatalytic activity. J. Solid State Chem. **183**(7), 1632–1639 (2010). https://doi.org/10.1016/j.jssc.2010.05.015

100. N.Y. Dzade, A. Roldan, N.H. de Leeuw, A density functional theory study of the adsorption of benzene on hematite (α-Fe_2O_3) surfaces. Minerals **4**(1), 89–115 (2014). https://doi.org/10.3390/min4010089

101. Y.-J. Zhu, S.-W. Cao, Hierarchically nanostructured r-Fe_2O_3 hollow spheres: preparation, growth mechanism, photocatalytic property, and application in water treatment. J. Phys. Chem. C **112**(16), 6253–6257 (2008). https://doi.org/10.1021/jp8000465

102. D. Su, X. Xie, S. Dou, G. Wang, CuO single crystal with exposed 001 facets-A highly efficient material for gas sensing and Li-ion battery applications. Sci. Rep. **4**, 5753 (2014). https://doi.org/10.1038/srep05753

103. F. Li, X. Liu, Q. Zhang, T. Kong, H. Jin, Fabrication and photocatalytic property of CuO nanosheets via a facile solution route. Cryst. Res. Technol. **47**(11), 1140–1147 (2012). https://doi.org/10.1002/crat.201200143

104. B. Peng, P.K. Ang, K.P. Loh, Two-dimensional dichalcogenides for light-harvesting applications. Nano Today **10**(2), 128–137 (2015). https://doi.org/10.1016/j.nantod.2015.01.007

105. M. Osada, T. Sasaki, Exfoliated oxide nanosheets: new solution to nanoelectronics. J. Mater. Chem. **19**(17), 2503–2511 (2009). https://doi.org/10.1039/b820160a

106. K. Kalantar-zadeh, A. Vijayaraghavan, M.-H. Ham, H. Zheng, M. Breedon, M.S. Strano, Synthesis of atomically thin WO_3 sheets from hydrated tungsten trioxide. Chem. Mater. **22**(19), 5660–5666 (2010). https://doi.org/10.1021/cm1019603

107. H. Ramakrishna Matte, A. Gomathi, A.K. Manna, D.J. Late, R. Datta, S.K. Pati, C. Rao, MoS_2 and WS_2 analogues of graphene. Angew. Chem. Int. Ed. **49**(24), 4059–4062 (2010). https://doi.org/10.1002/anie.201000009

108. M. Zhou, X.W.D. Lou, Y. Xie, Two-dimensional nanosheets for photoelectrochemical water splitting: possibilities and opportunities. Nano Today **8**(6), 598–618 (2013). https://doi.org/10.1016/j.nantod.2013.12.002

109. J. Mujtaba, H. Sun, F. Fang, M. Ahmad, J. Zhu, Fine control over the morphology and photocatalytic activity of 3D ZnO hierarchical nanostructures: capping vs. etching. RSC Adv.

5(69), 56232–56238 (2015). https://doi.org/10.1039/C5RA08325G

110. L. Zhang, H. Yang, J. Yu, F. Shao, L. Li, F. Zhang, H. Zhao, Controlled synthesis and photocatalytic activity of ZnSe nanostructured assemblies with different morphologies and crystalline phases. J. Phys. Chem. C **113**(14), 5434–5443 (2009). https://doi.org/10.1021/jp810385v

111. G. Tang, J. Sun, C. Wei, K. Wu, X. Ji, S. Liu, H. Tang, C. Li, Synthesis and characterization of flowerlike MoS_2 nanostructures through CTAB-assisted hydrothermal process. Mater. Lett. **86**(11), 9–12 (2012). https://doi.org/10.1016/j.matlet.2012.07.014

112. M. Zhong, Z. Wei, X. Meng, F. Wu, J. Li, From MoS_2 microspheres to α-MoO_3 nanoplates: growth mechanism and photocatalytic activities. Eur. J. Inorg. Chem. **2014**(20), 3245–3251 (2014). https://doi.org/10.1002/ejic.201402079

113. H. Zhang, Ultrathin two-dimensional nanomaterials. ACS Nano **9**(10), 9451–9469 (2015). https://doi.org/10.1021/acsnano.5b05040

114. R. Asahi, T. Morikawa, T. Ohwaki, K. Aoki, Y. Taga, Visible-light photocatalysis in nitrogen-doped titanium oxides. Science **293**(5528), 269–271 (2001). https://doi.org/10.1126/science.1061051

115. S. Bilmes, P. Mandelbaum, F. Alvarez, N. Victoria, Surface, electronic structure of titanium dioxide photocatalysts. J. Phys. Chem. B **104**(42), 9851–9858 (2000). https://doi.org/10.1021/jp0010132

116. N. Serpone, D. Lawless, J. Disdier, J.-M. Herrmann, Spectroscopic, photoconductivity, and photocatalytic studies of TiO_2 colloids: naked and with the lattice doped with Cr^{3+}, Fe^{3+}, and V^{5+} cations. Langmuir **10**(3), 643–652 (1994). https://doi.org/10.1021/la00015a010

117. P. Liu, Y. Liu, W. Ye, J. Ma, D. Gao, Flower-like n-doped MoS_2 for photocatalytic degradation of RhB by visible light irradiation. Nanotechnology **27**(22), 225403 (2016). https://doi.org/10.1088/0957-4484/27/22/225403

118. Q. Xiang, J. Yu, W. Wang, M. Jaroniec, Nitrogen self-doped nanosized TiO2 sheets with exposed 001 facets for enhanced visible-light photocatalytic activity. Chem. Commun. **47**(24), 6906–6908 (2011). https://doi.org/10.1039/c1cc11740h

119. B. Wang, M.K.H. Leung, X.-Y. Lu, S.-Y. Chen, Synthesis and photocatalytic activity of boron and fluorine codoped TiO_2 nanosheets with reactive facets. Appl. Energy **112**(16), 1190–1197 (2013). https://doi.org/10.1016/j.apenergy.2013.03.084

120. S. Liu, C. Li, J. Yu, Q. Xiang, Improved visible-light photocatalytic activity of porous carbon self-doped ZnO nanosheet-assembled flowers. CrystEngComm **13**(7), 2533 (2011). https://doi.org/10.1039/c0ce00295j

121. Y. Liu, S. Xie, H. Li, X. Wang, A highly efficient sunlight driven ZnO nanosheet photocatalyst: synergetic effect of P-doping and MoS_2 atomic layer loading. ChemCatChem **6**(9), 2522–2526 (2014). https://doi.org/10.1002/cctc.201402191

122. N. Li, H. Teng, L. Zhang, J. Zhou, M. Liu, Synthesis of Mo-doped WO_3 nanosheets with enhanced visible-light-driven photocatalytic properties. RSC Adv. **5**(115), 95394–95400 (2015). https://doi.org/10.1039/C5RA17098B

123. T. Jiang, J. Kong, Y. Wang, D. Meng, D. Wang, M. Yu, Optical and photocatalytic properties of Mn-doped CuO nanosheets prepared by hydrothermal method. Cryst. Res. Technol. **51**(1), 58–64 (2016). https://doi.org/10.1002/crat.201500152

124. M. Seifollahi Bazarjani, M. Hojamberdiev, K. Morita, G. Zhu, G. Cherkashinin et al., Visible light photocatalysis with c-$WO_{(3−x)}$/WO_3·H_2O nanoheterostructures in situ formed in mesoporous polycarbosilane-siloxane polymer. J. Am. Chem. Soc. **135**(11), 4467–4475 (2013). https://doi.org/10.1021/ja3126678

125. M.M. Alsaif, A.F. Chrimes, T. Daeneke, S. Balendhran, D.O. Bellisario et al., High-performance field effect transistors using electronic inks of 2D molybdenum oxide nanoflakes. Adv. Funct. Mater. **26**(1), 91–100 (2016). https://doi.org/10.1002/adfm.201503698

126. H. Cheng, T. Kamegawa, K. Mori, H. Yamashita, Surfactant-free nonaqueous synthesis of plasmonic molybdenum oxide nanosheets with enhanced catalytic activity for hydrogen generation from ammonia borane under visible light. Angew. Chem. Int. Ed. **53**(11), 2910–2914 (2014). https://doi.org/10.1002/anie.201309759

127. X. Tan, L. Wang, C. Cheng, X. Yan, B. Shen, J. Zhang, Plasmonic $MoO_{3−x}$@ MoO_3 nanosheets for highly sensitive SERS detection through nanoshell-isolated electromagnetic enhancement. Chem. Commun. **52**(14), 2893–2896 (2016). https://doi.org/10.1039/C5CC10020H

128. Y. Liao, Z. Hu, Q. Gu, C. Xue, Amine-functionalized ZnO nanosheets for efficient CO_2 capture and photoreduction. Molecules **20**(10), 18847–18855 (2015). https://doi.org/10.3390/molecules201018847

129. Y. Cho, W. Choi, C.-H. Lee, T. Hyeon, H.-I. Lee, Visible light-induced degradation of carbon tetrachloride on dye-sensitized TiO_2. Environ. Sci. Technol. **35**(5), 966–970 (2001). https://doi.org/10.1021/es001245e

130. K. Takanabe, K. Kamata, X. Wang, M. Antonietti, J. Kubota, K. Domen, Photocatalytic hydrogen evolution on dye-sensitized mesoporous carbon nitride photocatalyst with magnesium phthalocyanine. Phys. Chem. Chem. Phys. **12**(40), 13020–13025 (2010). https://doi.org/10.1039/c0cp00611d

131. Y. Yuan, H. Lu, Z. Ji, J. Zhong, M. Ding et al., Enhanced visible-light-induced hydrogen evolution from water in a noble-metal-free system catalyzed by $ZnTCPP$-MoS_2/TiO_2 assembly. Chem. Eng. J. **275**, 8–16 (2015). https://doi.org/10.1016/j.cej.2015.04.015

132. S. Mathew, A. Yella, P. Gao, R. Humphry-Baker, B.F. Curchod et al., Dye-sensitized solar cells with 13% efficiency achieved through the molecular engineering of porphyrin sensitizers. Nat. Chem. **6**(3), 242–247 (2014). https://doi.org/10.1038/nchem.1861

133. Y.-J. Yuan, J.-R. Tu, Z.-J. Ye, H.-W. Lu, Z.-G. Ji et al., Visible-light-driven hydrogen production from water in a noble-metal-free system catalyzed by zinc porphyrin sensitized MoS_2/ZnO. Dyes Pigm. **123**, 285–292 (2015). https://doi.org/10.1016/j.dyepig.2015.08.014

134. S. Min, G. Lu, Sites for high efficient photocatalytic hydrogen evolution on a limited-layered MoS_2 cocatalyst confined on graphene sheets-the role of graphene. J. Phys. Chem. C **116**(48), 25415–25424 (2012). https://doi.org/10.1021/jp3093786

135. T. Jafari, E. Moharreri, A.S. Amin, R. Miao, W. Song, S.L. Suib, Photocatalytic water splitting-the untamed dream: a review of recent advances. Molecules **21**(7), 900 (2016). https://doi.org/10.3390/molecules21070900

136. L. Ge, C. Han, X. Xiao, L. Guo, Synthesis and characterization of composite visible light active photocatalysts MoS_2–g-C_3N_4 with enhanced hydrogen evolution activity. Int. J. Hydrog. Energy **38**(17), 6960–6969 (2013). https://doi.org/10.1016/j.ijhydene.2013.04.006

137. M.Q. Wen, T. Xiong, Z.G. Zang, W. Wei, X.S. Tang, F. Dong, Synthesis of MoS_2/g-C_3N_4 nanocomposites with enhanced visible-light photocatalytic activity for the removal of nitric oxide (NO). Opt. Express **24**(10), 10205–10212 (2016). https://doi.org/10.1364/OE.24.010205

138. G.P. Awasthi, S.P. Adhikari, S. Ko, H.J. Kim, C.H. Park, C.S. Kim, Facile synthesis of ZnO flowers modified graphene like

MoS$_2$ sheets for enhanced visible-light-driven photocatalytic activity and antibacterial properties. J. Alloys Compd. **682**, 208–215 (2016). https://doi.org/10.1016/j.jallcom.2016.04.267

139. X. Li, H. Zhu, Two-dimensional MoS$_2$: properties, preparation, and applications. J. Materiomics **1**(1), 33–44 (2015). https://doi.org/10.1016/j.jmat.2015.03.003

140. L. Wei, Y. Chen, Y. Lin, H. Wu, R. Yuan, Z. Li, MoS$_2$ as non-noble-metal co-catalyst for photocatalytic hydrogen evolution over hexagonal ZnIn$_2$S$_4$ under visible light irradiations. Appl. Catal. B **144**(2), 521–527 (2014). https://doi.org/10.1016/j.apcatb.2013.07.064

141. Y.-J. Yuan, D.-Q. Chen, Y.-W. Huang, Z.-T. Yu, J.-S. Zhong et al., MoS$_2$ nanosheet-modified CuInS$_2$ photocatalyst for visible-light-driven hydrogen production from water. Chemsuschem **9**(9), 1003–1009 (2016). https://doi.org/10.1002/cssc.201600006

142. C. Liu, L. Wang, Y. Tang, S. Luo, Y. Liu, S. Zhang, Y. Zeng, Y. Xu, Vertical single or few-layer MoS$_2$ nanosheets rooting into TiO$_2$ nanofibers for highly efficient photocatalytic hydrogen evolution. Appl. Catal. B **164**, 1–9 (2015). https://doi.org/10.1016/j.apcatb.2014.08.046

143. X. Zhang, C. Shao, X. Li, F. Miao, K. Wang, N. Lu, Y. Liu, 3D MoS$_2$ nanosheet/TiO$_2$ nanofiber heterostructures with enhanced photocatalytic activity under UV irradiation. J. Alloys Compd. **686**, 137–144 (2016). https://doi.org/10.1016/j.jallcom.2016.05.336

144. Y. Min, G. He, Q. Xu, Y. Chen, Dual-functional MoS$_2$ sheet-modified CdS branch-like heterostructures with enhanced photostability and photocatalytic activity. J. Mater. Chem. A **2**(8), 2578 (2014). https://doi.org/10.1039/c3ta14240j

145. C. Wang, H. Lin, Z. Xu, H. Cheng, C. Zhang, One-step hydrothermal synthesis of flowerlike MoS$_2$/CdS heterostructures for enhanced visible-light photocatalytic activities. RSC Adv. **5**(20), 15621–15626 (2015). https://doi.org/10.1039/C4RA15632C

146. B. Zhu, B. Lin, Y. Zhou, P. Sun, Q. Yao, Y. Chen, B. Gao, Enhanced photocatalytic H$_2$ evolution on ZnS loaded with graphene and MoS$_2$ nanosheets as cocatalysts. J. Mater. Chem. A **2**(11), 3819 (2014). https://doi.org/10.1039/C3TA14819J

147. Y.J. Yuan, F. Wang, B. Hu, H.W. Lu, Z.T. Yu, Z.G. Zou, Significant enhancement in photocatalytic hydrogen evolution from water using a MoS$_2$ nanosheet-coated ZnO heterostructure photocatalyst. Dalton Trans. **44**(24), 10997–11003 (2015). https://doi.org/10.1039/C5DT00906E

148. N. Meng, Y. Zhou, W. Nie, L. Song, P. Chen, CuS/MoS$_2$ nanocomposite with high solar photocatalytic activity. J. Nanopart. Res. **17**(7), 300 (2015). https://doi.org/10.1007/s11051-015-3105-3

149. L. Gu, J. Wang, Z. Zou, X. Han, Graphitic-C$_3$N$_4$-hybridized TiO$_2$ nanosheets with reactive 001 facets to enhance the UV- and visible-light photocatalytic activity. J. Hazard Mater. **268**(6), 216–223 (2014). https://doi.org/10.1016/j.jhazmat.2014.01.021

150. Y. Hou, Y. Zhu, Y. Xu, X. Wang, Photocatalytic hydrogen production over carbon nitride loaded with WS$_2$ as cocatalyst under visible light. Appl. Catal. B **156**, 122–127 (2014). https://doi.org/10.1016/j.apcatb.2014.03.002

151. J. Fu, G. Li, F. Xi, X. Dong, Hybrid nanocomposite with visible-light photocatalytic activity: CdS-pillared titanate. Chem. Eng. J. **180**(3), 330–336 (2012). https://doi.org/10.1016/j.cej.2011.10.098

152. J. Zhang, Z. Zhu, Y. Tang, K. Müllen, X. Feng, Titania nanosheet-mediated construction of a two-dimensional titania/cadmium sulfide heterostructure for high hydrogen evolution activity. Adv. Mater. **26**(5), 734–738 (2014). https://doi.org/10.1002/adma.201303571

153. H.N. Kim, T.W. Kim, I.Y. Kim, S.-J. Hwang, Cocatalyst-free photocatalysts for efficient visible-light-induced H$_2$ production: porous assemblies of CdS quantum dots and layered titanate nanosheets. Adv. Funct. Mater. **21**(16), 3111–3118 (2011). https://doi.org/10.1002/adfm.201100453

154. F. Zheng, H. Lu, M. Guo, M. Zhang, Q. Zhen, Hydrothermal preparation of WO$_3$ nanorod array and ZnO nanosheet array composite structures on FTO substrates with enhanced photocatalytic properties. J. Mater. Chem. C **3**(29), 7612–7620 (2015). https://doi.org/10.1039/C5TC01125F

155. A.K. Kole, C.S. Tiwary, P. Kumbhakar, Ethylenediamine assisted synthesis of wurtzite zinc sulphide nanosheets and porous zinc oxide nanostructures: near white light photoluminescence emission and photocatalytic activity under visible light irradiation. CrystEngComm **15**(27), 5515–5525 (2013). https://doi.org/10.1039/c3ce40531a

156. X. Liu, J. Cao, B. Feng, L. Yang, M. Wei et al., Facile fabrication and photocatalytic properties of ZnO nanorods/ZnSe nanosheets heterostructure. Superlattices Microstruct. **83**, 447–458 (2015). https://doi.org/10.1016/j.spmi.2015.03.051

157. N. Huo, Q. Yue, J. Yang, S. Yang, J. Li, Abnormal photocurrent response and enhanced photocatalytic activity induced by charge transfer between WS$_2$ nanosheets and WO$_3$ nanoparticles. ChemPhysChem **14**(18), 4069–4073 (2013). https://doi.org/10.1002/cphc.201300680

158. Y. Sang, Z. Zhao, M. Zhao, P. Hao, Y. Leng, H. Liu, From UV to near-infrared, WS$_2$ nanosheet: a novel photocatalyst for full solar light spectrum photodegradation. Adv. Mater. **27**(2), 363–369 (2015). https://doi.org/10.1002/adma.201403264

159. X. Yu, J. Liu, Y. Yu, S. Zuo, B. Li, Preparation and visible light photocatalytic activity of carbon quantum dots/TiO$_2$ nanosheet composites. Carbon **68**, 718–724 (2014). https://doi.org/10.1016/j.carbon.2013.11.053

160. P. Atkin, T. Daeneke, Y. Wang, B. Carey, K. Berean et al., 2D WS$_2$/carbon dot hybrids with enhanced photocatalytic activity. J. Mater. Chem. A **4**(35), 13563–13571 (2016). https://doi.org/10.1039/C6TA06415A

161. S. Ida, A. Takashiba, S. Koga, H. Hagiwara, T. Ishihara, Potential gradient and photocatalytic activity of an ultrathin p–n junction surface prepared with two-dimensional semiconducting nanocrystals. J. Am. Chem. Soc. **136**(5), 1872–1878 (2014). https://doi.org/10.1021/ja409465k

162. F. Meng, J. Li, S.K. Cushing, M. Zhi, N. Wu, Solar hydrogen generation by nanoscale p–n junction of p-type molybdenum disulfide/n-type nitrogen-doped reduced graphene oxide. J. Am. Chem. Soc. **135**(28), 10286–10289 (2013). https://doi.org/10.1021/ja404851s

163. Z. Xing, X. Zong, Y. Zhu, Z. Chen, Y. Bai, L. Wang, A nanohybrid of CdTe@ CdS nanocrystals and titania nanosheets with p–n nanojunctions for improved visible light-driven hydrogen production. Catal. Today **264**, 229–235 (2016). https://doi.org/10.1016/j.cattod.2015.08.007

164. J. Zhang, J. Yu, Y. Zhang, Q. Li, J.R. Gong, Visible light photocatalytic H$_2$-production activity of CuS/ZnS porous nanosheets based on photoinduced interfacial charge transfer. Nano Lett. **11**(11), 4774–4779 (2011). https://doi.org/10.1021/nl202587b

165. Z.B. Yu, Y.P. Xie, G. Liu, G.Q. Lu, X.L. Ma, H.-M. Cheng, Self-assembled CdS/Au/ZnO heterostructure induced by surface polar charges for efficient photocatalytic hydrogen evolution. J. Mater. Chem. A **1**(8), 2773–2776 (2013). https://doi.org/10.1039/c3ta01476b

166. C. Zhu, L. Zhang, B. Jiang, J. Zheng, P. Hu, S. Li, M. Wu, W. Wu, Fabrication of Z-scheme Ag$_3$PO$_4$/MoS$_2$ composites with enhanced photocatalytic activity and stability for organic

pollutant degradation. Appl. Surf. Sci. **377**, 99–108 (2016). https://doi.org/10.1016/j.apsusc.2016.03.143

167. W.C. Peng, X. Wang, X.Y. Li, The synergetic effect of MoS_2 and graphene on Ag_3PO_4 for its ultra-enhanced photocatalytic activity in phenol degradation under visible light. Nanoscale **6**(14), 8311–8317 (2014). https://doi.org/10.1039/c4nr01654h

168. C. Wang, M. Wu, M. Yan, H. Shen, F. Cai, B. Hu, W. Shi, Enhanced visible-light photocatalytic activity and the mechanism study of WO_3 nanosheets coupled with Ag_3PO_4 nanocrystals. Ceram. Int. **41**(5), 6784–6792 (2015). https://doi.org/10.1016/j.ceramint.2015.01.125

169. W. Tu, Y. Zhou, S. Feng, Q. Xu, P. Li, X. Wang, M. Xiao, Z. Zou, Hollow spheres consisting of $Ti_{0.91}O_2$/CdS nanohybrids for CO_2 photofixation. Chem. Commun. **51**(69), 13354–13357 (2015). https://doi.org/10.1039/C5CC03905C

170. K. Schierbaum, U. Kirner, J. Geiger, W. Göpel, Schottky-barrier and conductivity gas sensors based upon Pd/SnO_2 and Pt/TiO_2. Sens. Actuator-B Chem. **4**(1), 87–94 (1991). https://doi.org/10.1016/0925-4005(91)80181-I

171. A.L. Linsebigler, G. Lu, J.T. Yates, Photocatalysis on TiO_2 surfaces: principles, mechanisms, and selected results. Chem. Rev. **95**(3), 735–758 (1995). https://doi.org/10.1021/cr00035a013

172. Y. Gao, W. Lee, R. Trehan, R. Kershaw, K. Dwight, A. Wold, Improvement of photocatalytic activity of titanium (IV) oxide by dispersion of Au on TiO_2. Mater. Res. Bull. **26**(12), 1247–1254 (1991). https://doi.org/10.1016/0025-5408(91)90138-C

173. V. Subramanian, E.E. Wolf, P.V. Kamat, Catalysis with TiO_2/gold nanocomposites. Effect of metal particle size on the Fermi level equilibration. J. Am. Chem. Soc. **126**(15), 4943–4950 (2004). https://doi.org/10.1021/ja0315199

174. Y. Liang, N. Guo, L. Li, R. Li, G. Ji, S. Gan, Fabrication of porous 3D flower-like Ag/ZnO heterostructure composites with enhanced photocatalytic performance. Appl. Surf. Sci. **332**, 32–39 (2015). https://doi.org/10.1016/j.apsusc.2015.01.116

175. A.J. Cheah, W.S. Chiu, P.S. Khiew, H. Nakajima, T. Saisopa, P. Songsiriritthigul, S. Radiman, M.A.A. Hamid, Facile synthesis of a Ag/MoS_2 nanocomposite photocatalyst for enhanced visible-light driven hydrogen gas evolution. Catal. Sci. Technol. **5**(8), 4133–4143 (2015). https://doi.org/10.1039/C5CY00464K

176. D. Zhang, X. Liu, X. Wang, Growth and photocatalytic activity of ZnO nanosheets stabilized by Ag nanoparticles. J. Alloys Compd. **509**(15), 4972–4977 (2011). https://doi.org/10.1016/j.jallcom.2011.01.145

177. Y. Xin, L. Wu, L. Ge, C. Han, Y. Li, S. Fang, Gold-palladium bimetallic nanoalloy decorated ultrathin 2D TiO_2 nanosheets as efficient photocatalysts with high hydrogen evolution activity. J. Mater. Chem. A **3**(16), 8659–8666 (2015). https://doi.org/10.1039/C5TA00759C

178. L. Yang, D. Zhong, J. Zhang, Z. Yan, S. Ge et al., Optical properties of metal-molybdenum disulfide hybrid nanosheets and their application for enhanced photocatalytic hydrogen evolution. ACS Nano **8**(7), 6979–6985 (2014). https://doi.org/10.1021/nn501807y

179. S. Sakthivel, M. Shankar, M. Palanichamy, B. Arabindoo, D. Bahnemann, V. Murugesan, Enhancement of photocatalytic activity by metal deposition: characterisation and photonic efficiency of Pt, Au and Pd deposited on TiO_2 catalyst. Water Res. **38**(13), 3001–3008 (2004). https://doi.org/10.1016/j.watres.2004.04.046

180. Y. Homma, Y. Kobayashi, T. Ogino, D. Takagi, R. Ito, Y.J. Jung, P.M. Ajayan, Role of transition metal catalysts in single-walled carbon nanotube growth in chemical vapor deposition. J. Phys. Chem. B **107**(44), 12161–12164 (2003). https://doi.org/10.1021/jp0353845

181. Y. Wu, M. Xu, X. Chen, S. Yang, H. Wu, J. Pan, X. Xiong, CTAB-assisted synthesis of novel ultrathin $MoSe_2$ nanosheets perpendicular to graphene for the adsorption and photodegradation of organic dyes under visible light. Nanoscale **8**(1), 440–450 (2016). https://doi.org/10.1039/C5NR05748E

182. S. Kong, S. Jin, H. Liu, Y. Wang, Morphological effect of graphene nanosheets on ultrathin CoS nanosheets and their applications for high-performance Li-ion batteries and photocatalysis. J. Phys. Chem. C **118**(44), 25355–25364 (2014). https://doi.org/10.1021/jp508698q

183. W. Guo, F. Zhang, C. Lin, Z.L. Wang, Direct growth of TiO_2 nanosheet arrays on carbon fibers for highly efficient photocatalytic degradation of methyl orange. Adv. Mater. **24**(35), 4761–4764 (2012). https://doi.org/10.1002/adma.201201075

184. T. Daeneke, N. Dahr, P. Atkin, R.M. Clark, C.J. Harrison, et al., Surface water dependent properties of sulfur-rich molybdenum sulfides: electrolyteless gas phase water splitting. ACS Nano **11**(7), 6782–6794 (2017). http://pubs.acs.org/doi/abs/10.1021/acsnano.7b01632

185. J. Sun, H. Zhang, L.-H. Guo, L. Zhao, Two-dimensional interface engineering of a titania-graphene nanosheet composite for improved photocatalytic activity. ACS Appl. Mater. Interfaces **5**(24), 13035–13041 (2013). https://doi.org/10.1021/am403937y

186. Y. Zhang, Z.-R. Tang, X. Fu, Y.-J. Xu, Engineering the unique 2D mat of graphene to achieve graphene-TiO_2 nanocomposite for photocatalytic selective transformation: what advantage does graphene have over its forebear carbon nanotube. ACS Nano **5**(9), 7426–7435 (2011). https://doi.org/10.1021/nn202519j

187. W. Tu, Y. Zhou, Q. Liu, Z. Tian, J. Gao, X. Chen, H. Zhang, J. Liu, Z. Zou, Robust hollow spheres consisting of alternating titania nanosheets and graphene nanosheets with high photocatalytic activity for CO_2 conversion into renewable fuels. Adv. Funct. Mater. **22**(6), 1215–1221 (2012). https://doi.org/10.1002/adfm.201102566

188. S. Bai, L. Wang, X. Chen, J. Du, Y. Xiong, Chemically exfoliated metallic MoS_2 nanosheets: a promising supporting cocatalyst for enhancing the photocatalytic performance of TiO_2 nanocrystals. Nano Res. **8**(1), 175–183 (2014). https://doi.org/10.1007/s12274-014-0606-9

189. R. Bera, S. Kundu, A. Patra, 2D hybrid nanostructure of reduced graphene oxide-CdS nanosheet for enhanced photocatalysis. ACS Appl. Mater. Interfaces **7**(24), 13251–13259 (2015). https://doi.org/10.1021/acsami.5b03800

190. D. Chen, T. Li, Q. Chen, J. Gao, B. Fan, J. Li, X. Li, R. Zhang, J. Sun, L. Gao, Hierarchically plasmonic photocatalysts of Ag/AgCl nanocrystals coupled with single-crystalline WO_3 nanoplates. Nanoscale **4**(17), 5431–5439 (2012). https://doi.org/10.1039/c2nr31030a

191. Z. Zhang, J. Huang, M. Zhang, Q. Yuan, B. Dong, Ultrathin hexagonal SnS_2 nanosheets coupled with gC_3N_4 nanosheets as 2D/2D heterojunction photocatalysts toward high photocatalytic activity. Appl. Catal. B **163**(163), 298–305 (2015). https://doi.org/10.1016/j.apcatb.2014.08.013

192. X. Yang, H. Xue, J. Xu, X. Huang, J. Zhang et al., Synthesis of porous $ZnS:Ag_2S$ nanosheets by ion exchange for photocatalytic H_2 generation. ACS Appl. Mater. Interfaces **6**(12), 9078–9084 (2014). https://doi.org/10.1021/am5020953

193. Y.-J. Yuan, Z.-J. Ye, H.-W. Lu, B. Hu, Y.-H. Li, D.-Q. Chen, J.-S. Zhong, Z.-T. Yu, Z.-G. Zou, Constructing anatase TiO_2 nanosheets with exposed (001) facets/layered MoS_2 two-dimensional nanojunctions for enhanced solar hydrogen generation. ACS Catal. **6**(2), 532–541 (2016). https://doi.org/10.1021/acscatal.5b02036

194. X. Zong, H. Yan, G. Wu, G. Ma, F. Wen, L. Wang, C. Li, Enhancement of photocatalytic H_2 evolution on CdS by loading MoS_2 as cocatalyst under visible light irradiation. J. Am. Chem.

Soc. **130**(23), 7176–7177 (2008). https://doi.org/10.1021/ja8007825

195. X. Han, Q. Kuang, M. Jin, Z. Xie, L. Zheng, Synthesis of titania nanosheets with a high percentage of exposed (001) facets and related photocatalytic properties. J. Am. Chem. Soc. **131**(9), 3152–3153 (2009). https://doi.org/10.1021/ja8092373

196. L. Yang, X. Kong, J. Wang, M. Pan, W. Yang, J. Yang, W. Jiang, Synthesis and photocatalytic performance of ZnO hollow spheres and porous nanosheets. J. Mater. Sci. Mater. El. **27**(1), 203–209 (2015). https://doi.org/10.1007/s10854-015-3738-0

197. M. Tanveer, C. Cao, Z. Ali, I. Aslam, F. Idrees, W.S. Khan, F.K. But, M. Tahir, N. Mahmood, Template free synthesis of CuS nanosheet-based hierarchical microspheres: an efficient natural light driven photocatalyst. CrystEngComm **16**(24), 5290 (2014). https://doi.org/10.1039/c4ce00090k

198. Y. Wen, Y. Zhu, S. Zhang, Low temperature synthesis of ZrS_2 nanoflakes and their catalytic activity. RSC Adv. **5**(81), 66082–66085 (2015). https://doi.org/10.1039/C5RA12412C

199. T. Lin, J. Wang, L. Guo, F. Fu, Fe_3O_4@MoS_2 core-shell composites: preparation, characterization, and catalytic application. J. Phys. Chem. C **119**(24), 13658–13664 (2015). https://doi.org/10.1021/acs.jpcc.5b02516

200. M. Tou, Z. Luo, S. Bai, F. Liu, Q. Chai, S. Li, Z. Li, Sequential coating upconversion NaYF4:Yb, Tm nanocrystals with SiO_2 and ZnO layers for NIR-driven photocatalytic and antibacterial applications. Mater. Sci. Eng. C **70**(Pt 2), 1141–1148 (2016). https://doi.org/10.1016/j.msec.2016.03.038

201. K. Kamaraj, R.P. George, B. Anandkumar, N. Parvathavarthini, U. Kamachi Mudali, A silver nanoparticle loaded TiO_2 nanoporous layer for visible light induced antimicrobial applications. Bioelectrochemistry **106**(Pt B), 290–297 (2015). https://doi.org/10.1016/j.bioelechem.2015.07.005

202. W. Wu, C. Jiang, V.A. Roy, Recent progress in magnetic iron oxide-semiconductor composite nanomaterials as promising photocatalysts. Nanoscale **7**(1), 38–58 (2015). https://doi.org/10.1039/C4NR04244A

203. M.T. Greiner, M.G. Helander, W.-M. Tang, Z.-B. Wang, J. Qiu, Z.-H. Lu, Universal energy-level alignment of molecules on metal oxides. Nat. Mater. **11**(1), 76–81 (2012). https://doi.org/10.1038/nmat3159

204. R. van de Krol, Y. Liang, J. Schoonman, Solar hydrogen production with nanostructured metal oxides. J. Mater. Chem. **18**(20), 2311–2320 (2008). https://doi.org/10.1039/b718969a

205. M.T. Greiner, Z.-H. Lu, Thin-film metal oxides in organic semiconductor devices: their electronic structures, work functions and interfaces. NPG Asia Mater. **5**(7), 547–556 (2013). https://doi.org/10.1038/am.2013.29

206. Y. Xu, M.A. Schoonen, The absolute energy positions of conduction and valence bands of selected semiconducting minerals. Am. Mineral. **85**(3), 543–556 (2000). https://doi.org/10.2138/am-2000-0416

207. J. Lim, W.K. Bae, J. Kwak, S. Lee, C. Lee, K. Char, Perspective on synthesis, device structures, and printing processes for quantum dot displays. Opt. Mater. Express **2**(5), 594–628 (2012). https://doi.org/10.1364/OME.2.000594

208. M. Thripuranthaka, R.V. Kashid, C. Sekhar Rout, D.J. Late, Temperature dependent Raman spectroscopy of chemically derived few layer MoS_2 and WS_2 nanosheets. Appl. Phys. Lett. **104**(8), 081911 (2014). https://doi.org/10.1063/1.4866782

209. R. Das, S. Pandey, Comparison of optical properties of bulk and nano crystalline thin films of CdS using different precursors. Int. J. Mater. Sci. **1**(1), 35–40 (2011). http://www.dpi-journals.com/index.php/IJMSCI/article/view/881/749

210. S. Balendhran, J. Deng, J.Z. Ou, S. Walia, J. Scott, J. Tang, K.L. Wang, M.R. Field, S. Russo, S. Zhuiykov, Enhanced charge carrier mobility in two-dimensional high dielectric molybdenum oxide. Adv. Mater. **25**(1), 109–114 (2013). https://doi.org/10.1002/adma.201203346

211. J. Zheng, H. Zhang, S. Dong, Y. Liu, C.T. Nai, H.S. Shin, H.Y. Jeong, B. Liu, K.P. Loh, High yield exfoliation of two-dimensional chalcogenides using sodium naphthalenide. Nat. Commun. **5**(1), 2995 (2014). https://doi.org/10.1038/ncomms3995

212. Y. Zhang, S. Liu, W. Liu, T. Liang, X. Yang, M. Xu, H. Chen, Two-dimensional MoS_2-assisted immediate aggregation of poly-3-hexylthiophene with high mobility. Phys. Chem. Chem. Phys. **17**(41), 27565–27572 (2015). https://doi.org/10.1039/C5CP05011A

213. X. Xiao, H. Song, S. Lin, Y. Zhou, X. Zhan et al., Scalable salt-templated synthesis of two-dimensional transition metal oxides. Nat. Commun. **7**, 11296 (2016). https://doi.org/10.1038/ncomms11296

214. R. Das, H. Mishra, A. Srivastava, A.M. Kayastha, Covalent immobilization of β-amylase onto functionalized molybdenum sulfide nanosheets, its kinetics and stability studies: a gateway to boost enzyme application. Chem. Eng. J. **328**, 215–227 (2017). https://doi.org/10.1016/j.cej.2017.07.019

215. S.S. Lo, T. Mirkovic, C.H. Chuang, C. Burda, G.D. Scholes, Emergent properties resulting from type-II band alignment in semiconductor nanoheterostructures. Adv. Mater. **23**(2), 180–197 (2011). https://doi.org/10.1002/adma.201002290

216. R. Zha, R. Nadimicherla, X. Guo, Ultraviolet photocatalytic degradation of methyl orange by nanostructured TiO_2/ZnO heterojunctions. J. Mater. Chem. A **3**(12), 6565–6574 (2015). https://doi.org/10.1039/C5TA00764J